Supporting Information

Spin Delocalization in the Radical Cations of Porphyrin Molecular Wires: A New Perspective on EPR Approaches

Gabriel Moise,[†,§] Lara Tejerina,[‡,§] Michel Rickhaus,[‡] Harry L. Anderson,[*,‡] and Christiane R. Timmel[*,†]

[†] Centre for Advanced Electron Spin Resonance, Department of Chemistry, University of Oxford, Oxford, OX1 3QR, UK

[‡] Chemistry Research Laboratory, Department of Chemistry, University of Oxford, Oxford, OX1 3TA, UK

[§] These authors contributed equally

Contents

Materials and General Methods

The zinc porphyrin oligomers ***l*-P1**, ***l*-P5**, and ***c*-P6·T6** depicted in Figure 1 of the main text were synthesized according to previously published procedures.[1,2] All manipulations of air- or water-sensitive compounds were performed using standard high-vacuum techniques. Commercially available reagents were used without further purification unless otherwise noted. Tris(4-bromophenyl)ammoniumyl hexachloroantimonate (BAHA) was purchased from Fluka and recrystallized from CH_2Cl_2 / petroleum ether$_{40–60}$. Dry solvents were obtained from the solvent drying system MBraun MB-SPS-5-BenchTop under nitrogen atmosphere (H_2O content < 20 ppm as determined by Karl-Fischer titration). Anhydrous $CHCl_3$ was purchased from Aldrich containing 0.5 – 1.0 % (v/v) of ethanol as stabilizer. Unless specified otherwise, all other solvents were used as commercially supplied.

Flash chromatography was carried out on silica gel 60 under positive pressure. Analytical thin-layer chromatography was carried out on aluminum-backed silica gel 60 F254 plates. Visualization was achieved using UV light when necessary.

Size exclusion chromatography (SEC) was carried out using Bio-Beads S-X1, 200-400 mesh (Bio Rad). Analytical GPC was carried out using JAIGEL-3H-A (8ϕ × 500) and JAIGEL-4H-A (8ϕ × 500) columns in THF + 1% pyridine as eluent with a flow rate of 1.0 mL/min. Analytical and semi-preparative GPC were also carried out on a Shimadzu Recycling GPC system equipped with a LC-20 AD pump, SPD-20A UV detector and a set of JAIGEL 3H (20 × 600 mm) and JAIGEL 4H (20 × 600 mm) columns in toluene + 1% pyridine as the eluent at a flow rate of 3.5 mL/min.

All UV-vis-NIR spectra were recorded in solution using a Perkin-Lambda 20 spectrometer (1 cm path length quartz cell).

$^{1}H/^{13}C$ NMR spectra were recorded at 298 K using a Bruker AV400 (400/100 MHz) instrument. NMR spectra are reported in ppm; coupling constants are given in Hertz to the nearest 0.1 Hz. The solvent used was $CDCl_3$ which was calibrated to residual $CHCl_3$ at 7.26 ppm.

MALDI-ToF spectra were measured at the EPSRC National Mass Spectrometry service (Swansea) using the Applied Biosystems Voyager DE-STR or at the University of Oxford using a Bruker AutoFlex Speed MALDI-TOF utilizing *trans*-2-[3-(4-*tert*-butylphenyl)-2-methyl-2-propenylidene]malononitrile (DCTB) as a matrix.

Chemical Oxidation

Samples for the EPR measurements were prepared in d_8-toluene:d_8-THF:CD_2Cl_2 1:1:1 and de-oxygentaed using several freeze-pump-thaw cycles. For chemical oxidation, ~0.5 equiv. of BAHA (1.0 mM in CD_2Cl_2) were added to a solution of porphyrin oligomer (~0.1 mM in d_8-toluene:d_8-THF:CD_2Cl_2 1:1:1) under argon just before the EPR measurements. The samples were prepared either in X-band tubes (3.8 mm o.d.) or Q-band tubes (2.0 mm o.d.) for the respective measurements. For the low-temperature measurements the samples were then frozen in liquid nitrogen.

Synthetic Procedures

Synthesis of *l*-P2

Scheme S1 depicts the synthetic route followed for the preparation of ***l*-P2**. Monomers **1** and **2** were prepared as reported previously.[2]

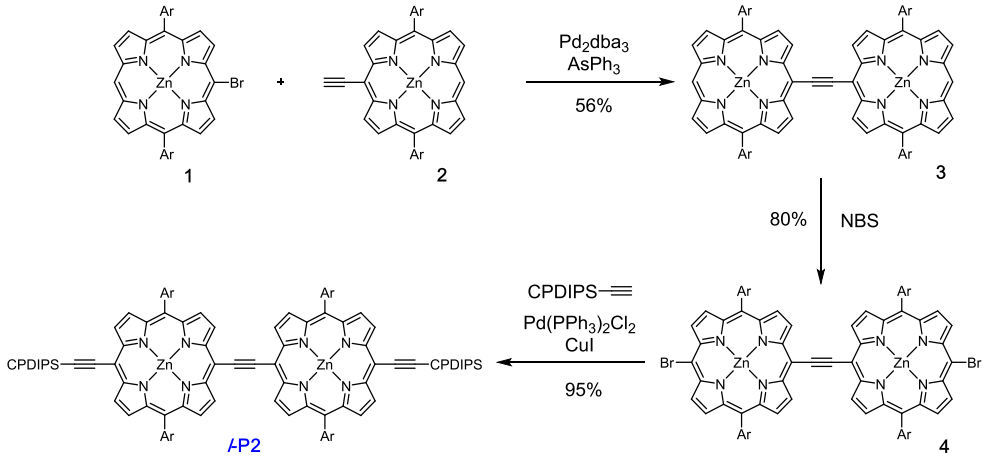

Scheme S1. Synthetic route for ***l*-P2**. Ar = 3,5-bis(trihexylsilyl)phenyl. CPDIPS = cyanopropyl-diisopropyl-silyl.

Porphyrin dimer **3**:

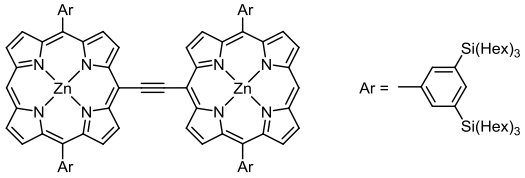

To a dried, argon flushed Schlenk-tube was added **1** (200 mg, 0.11 mmol) and **2** (194 mg, 0.11 mmol) together with dry THF (33 mL) and dry NEt_3 (4 mL) before performing two consecutive freeze-pump-thaw cycles. While frozen, $Pd_2(dba)_3$ (21 mg, 23 µmol) and $AsPh_3$ (51 mg, 0.17 mmol) were added under a stream of argon, before performing three additional freeze-pump-thaw cycles. The solution was heated to 50 °C for 2 d before cooling to room temperature and removing the solvents under reduced pressure. A short plug (NEt_3-deactivated SiO_2; $PE_{40–60}/CH_2Cl_2$ 10:1), and subsequent short SEC (toluene + 1% pyridine) and recycling GPC (toluene + 1% pyridine) yielded **3** (215 mg, 56%) as a dark brown oily solid.

^{1}H NMR (400 MHz, $CDCl_3$, 298 K): δ_H 10.46 (d, *J* = 4.4 Hz, 4H, H_β), 10.20 (s, 2H, H_{meso}), 9.33 (d, *J* = 4.4 Hz, 4H, H_β), 9.15 (d, *J* = 4.4 Hz, 4H, H_β), 9.01 (d, *J* = 4.4 Hz, 4H, H_β), 8.35 (s, 8H, H_{Ar}), 8.00 (s, 4H, H_{Ar}), 1.52 – 0.79 (m, 312H, H_{Hex}) ppm.

MALDI-ToF *m/z* 3335 (calculated for $[C_{210}H_{342}N_8Si_8Zn_2]^+$: 3334.5).

UV-vis-NIR (toluene) λ_{max} (log ε): 678 (4.63), 558 (4.31), 480 (5.45), 4.13 (5.15).

Porphyrin dimer **4**:

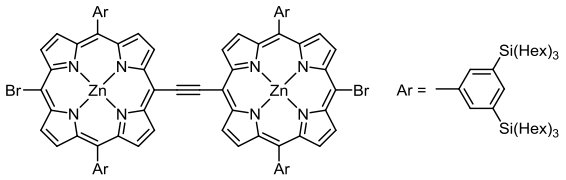

Dimer **3** (128 mg, 38 µmol) was placed in a round-bottom flask. Argon-saturated dry ethanol-stabilized $CHCl_3$ (6 mL), and dry pyridine (2.5 mL) were added before cooling to –78 °C. In a second flask, a solution of NBS (15 mg, 84 µmol) in argon-degassed dry ethanol-stabilized $CHCl_3$ (19 mL) was prepared and subsequently added to the first solution over 30 min at –78 °C. Stirring was continued for an additional 10 min at –78 °C. The solution was allowed to warm to –41 °C, and stirred for 1 h. Finally, the reaction mixture was placed in an ice bath at 0 °C for 15 min. The reaction mixture was subjected directly to a short plug (SiO_2; $PE_{40–60}/CH_2Cl_2$ 10:1) yielding **4** (107 mg, 80%) as a dark brown oily solid.

^{1}H NMR (400 MHz, $CDCl_3$, 298 K): δ_H 10.30 (d, *J* = 4.4 Hz, 4H, H_β), 9.65 (d, *J* = 4.4 Hz, 4H, H_β), 9.00 (d, *J* = 4.4 Hz, 4H, H_β), 8.33 (d, *J* = 4.4 Hz, 4H, H_β), 8.27 (s, 8H, H_{Ar}), 7.98 (s, 4H, H_{Ar}), 1.57 – 0.79 (m, 312H, H_{Hex}) ppm.

MALDI-ToF *m/z* 3493 (calculated for $[C_{210}H_{340}Br_2N_8Si_8Zn_2]^+$: 3492.3).

UV-vis-NIR (toluene) λ_{max} (log ε): 696 (4.74), 558 (4.29), 483 (5.49), 419 (5.18).

Porphyrin dimer ***l*-P2**:

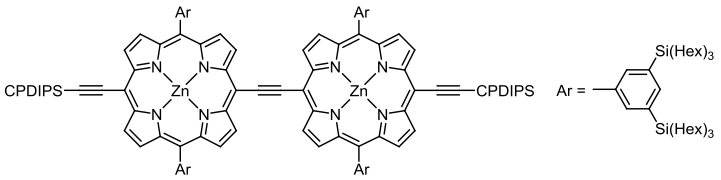

Dimer **4** (24 mg, 7 µmol) was placed in an argon flushed Schlenk flask. Dry toluene (0.5 mL) and dry *i*-Pr_2NH (0.5 mL) were added. 3-Cyanopropyldiisopropylsilylacetylene (7.1 mg, 7.2 µL, 34 µmol) was added. The solution was freeze-pump-thaw degassed (3 cycles). While frozen, catalysts $Pd(PPh_3)_2Cl_2$ (1.0 mg, 1.4 µmol) and CuI (0.13 mg, 0.7 µmol) were added under a stream of argon, before performing three additional freeze-pump-thaw cycles. The solution was stirred at 50 °C for 2 h before cooling to room temperature and removing the solvents under reduced pressure. The residue was subjected to a plug (SiO_2; CH_2Cl_2) giving target porphyrin ***l*-P2** (24 g, 95%) as a dark brown oily solid.

^{1}H NMR (400 MHz, $CDCl_3$, 298 K): δ_H 10.35 (d, *J* = 4.4 Hz, 4H, H_β), 9.73 (d, *J* = 4.4 Hz, 4H, H_β), 9.06 (d, *J* = 4.4 Hz, 4H, H_β), 8.95 (d, *J* = 4.4 Hz, 4H, H_β), 8.30 (s, 8H, H_{Ar}), 8.01 (s, 4H, H_{Ar}), 2.57 (t, *J* = 6.8 Hz, 4H, H_{CPDIPS}), 2.26 – 2.18 (m, 4H, H_{CPDIPS}), 1.53 – 0.79 (m, 344H, $H_{Hex/CPDIPS}$) ppm.

^{13}C NMR (100 MHz, $CDCl_3$, 298 K): δ_C 152.7, 152.6, 150.8, 140.4, 140.3, 139.5, 135.1, 133.4, 131.2, 131.0, 124.6, 119.8, 110.3, 103.2, 101.1, 100.2, 97.1, 33.6, 31.7, 29.9, 24.2, 22.8, 22.7, 21.8, 21.2, 18.8, 18.5, 14.3, 12.8, 12.5, 10.3, 1.2 ppm.

MALDI-ToF *m/z* 3746 (calculated for $[C_{234}H_{380}N_{10}Si_{10}Zn_2]^+$: 3745.2).

UV-vis-NIR (toluene) λ_{max} (log ε): 721 (4.83), 573 (4.23), 489 (5.44), 452 (5.17), 425 (5.16).

Synthesis of *l*-P3 and *l*-P4

Scheme S2 depicts the synthetic routes followed for the preparation of ***l*-P3** and ***l*-P4**. Trimer **5** and monomer **6** were prepared as reported previously.[1-3]

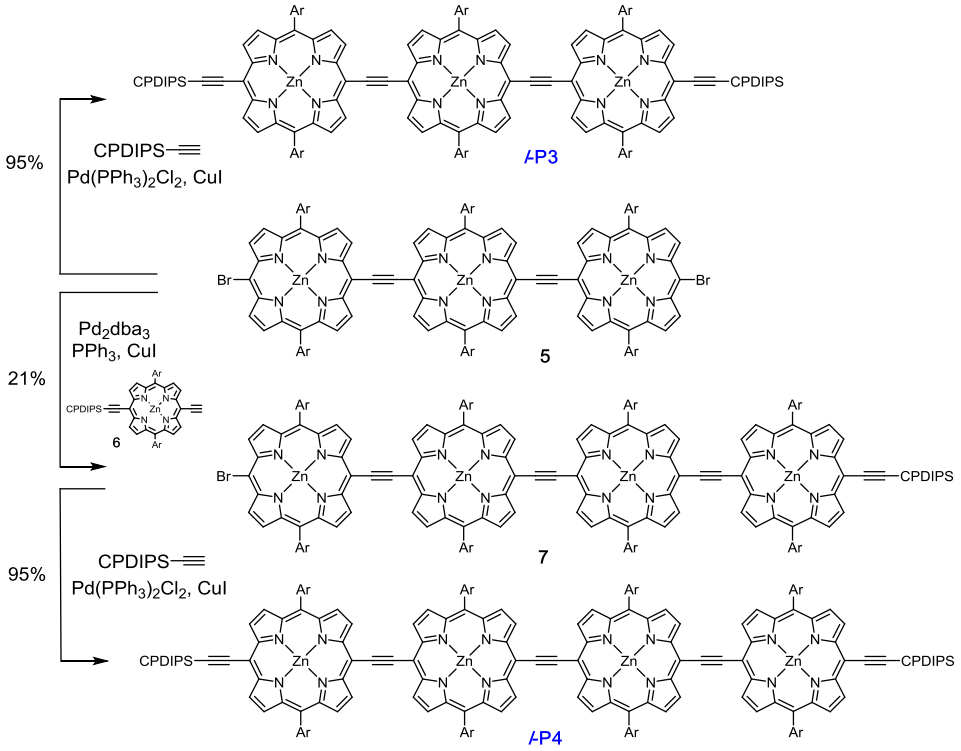

Scheme S2. Synthetic routes for ***l*-P3** and ***l*-P4**. Ar = 3,5-bis(trihexylsilyl)phenyl. CPDIPS = cyanopropyl-diisopropyl-silyl.

Porphyrin trimer ***l*-P3**:

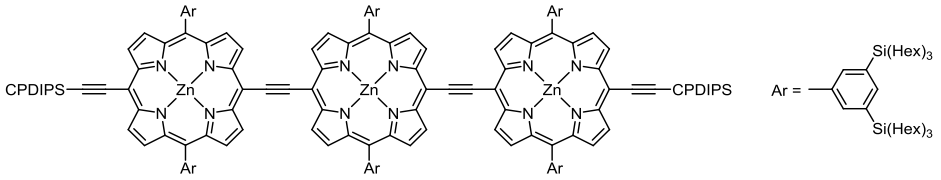

Trimer **5** (137 mg, 26 µmol) was placed in an argon flushed Schlenk flask. Dry toluene (0.5 mL) and dry *i*-Pr_2NH (0.5 mL) were added. 3-Cyanopropyldiisopropylsilylacetylene (27 mg, 27.5 µL, 0.13 mmol) was added. The solution was freeze-pump-thaw degassed (3 cycles). While frozen, catalysts $Pd(PPh_3)_2Cl_2$ (3.65 mg, 5.2 µmol) and CuI (0.49 mg, 2.6 µmol) were added under a stream of argon, before performing three additional freeze-pump-thaw cycles. The solution was stirred at 50 °C for 2 h before cooling to room temperature and removing the solvents under reduced pressure. The residue was subjected to a plug (SiO_2; CH_2Cl_2) giving target porphyrin ***l*-P3** (136 mg, 95%) as a dark brown oily solid.

^{1}H NMR (400 MHz, $CDCl_3$, 298 K): δ_H 10.39 – 10.37 (m, 8H, H_β), 9.72 (d, *J* = 4.8 Hz, 4H, H_β), 9.10 – 9.07 (m, 8H, H_β), 8.95 (d, *J* = 4.8 Hz, 4H, H_β), 8.39 (s, 4H, H_{Ar}), 8.32 (s, 8H, H_{Ar}), 8.04 (s, 6H, H_{Ar}), 2.58 (t, *J* = 6.8 Hz, 4H, H_{CPDIPS}), 2.26 – 2.18 (m, 4H, H_{CPDIPS}), 1.54 – 0.73 (m, 500H, $H_{CPDIPS/Hex}$) ppm.

MALDI-ToF *m/z* 5421 (calculated for $[C_{340}H_{550}N_{14}Si_{14}Zn_3]^+$: 5423.5).

UV-vis-NIR (toluene) λ_{max} (log ε): 765 (5.06), 583 (4.30), 491 (5.37), 450 (5.32).

Porphyrin tetramer **7**:

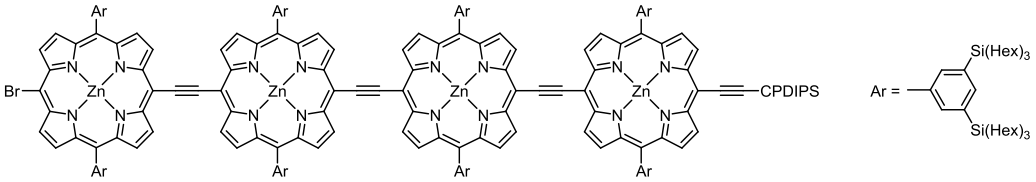

To a dried, argon flushed Schlenk-tube was added **5** (100 mg, 19.3 µmol) and **6** (55 mg, 29.2 µmol) together with dry toluene (10 mL) and dry *i*-Pr_2NH (10 mL) before performing two consecutive freeze-pump-thaw cycles. While frozen, $Pd_2(dba)_3$ (11 mg, 12 µmol), PPh_3 (2.0 mg, 7.6 µmol) and CuI (0.9 mg, 4.7 µmol) were added under a stream of argon, before performing three additional freeze-pump-thaw cycles. The solution was heated to 50 °C for 2 d before cooling to room temperature and removing the solvents under reduced pressure. A short plug (NEt_3-deactivated SiO_2; $PE_{40–60}/CH_2Cl_2$ 1:1), and subsequent short SEC (toluene + 1% pyridine) and recycling GPC (toluene + 1% pyridine) yielded **7** (28 mg, 21%) as a dark brown oily solid.

^{1}H NMR (400 MHz, $CDCl_3$, 298 K): δ_H 10.39 – 10.35 (m, 12H, H_β), 9.71 (d, *J* = 4.8 Hz, 2H, H_β), 9.62 (d, *J* = 4.8 Hz, 2H, H_β), 9.09 – 9.04 (m, 12H, H_β), 8.92 (d, *J* = 4.8 Hz, 2H, H_β), 8.91 (d, *J* = 4.8 Hz, 2H, H_β), 8.38 (s, 8H, H_{Ar}), 8.21 (s, 8H, H_{Ar}), 8.03 (s, 4H, H_{Ar}), 8.02 (s, 4H, H_{Ar}), 2.57 (t, *J* = 7.2 Hz, 2H, H_{CPDIPS}), 2.27 – 2.19 (m, 2H, H_{CPDIPS}), 1.55 – 0.74 (m, 640H, $H_{CPDIPS/Hex}$) ppm.

MALDI-ToF *m/z* 6973 (calculated for $[C_{434}H_{700}BrN_{17}Si_{17}Zn_4]^+$: 6975.3).

Porphyrin tetramer ***I*-P4**:

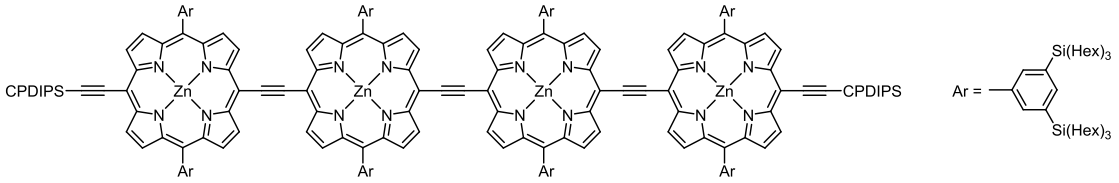

Tetramer **7** (21 mg, 3 µmol) was placed in an argon flushed Schlenk flask. Dry toluene (0.5 mL) and dry *i*-Pr_2NH (0.5 mL) were added. 3-Cyanopropyldiisopropylsilylacetylene (3.1 mg, 3.2 µL, 15 µmol) was added. The solution was freeze-pump-thaw degassed (3 cycles). While frozen, catalysts $Pd(PPh_3)_2Cl_2$ (0.4 mg, 0.6 µmol) and CuI (0.06 mg, 0.3 µmol) were added under a stream of argon, before performing three additional freeze-pump-thaw cycles. The solution was stirred at 50 °C for 2 h before cooling to room temperature and removing the solvents under reduced pressure. The residue was subjected to a plug (SiO_2; CH_2Cl_2) giving target porphyrin ***I*-P4** (20 mg, 95%) as a dark brown oily solid.

^{1}H NMR (400 MHz, $CDCl_3$, 298 K): δ_H 10.40 – 10.37 (m, 12H, H_β), 9.71 (d, *J* = 4.8 Hz, 4H, H_β), 9.10 – 9.06 (m, 12H, H_β), 8.95 (d, *J* = 4.8 Hz, 4H, H_β), 8.40 (s, 8H, H_{Ar}), 8.32 (s, 8H, H_{Ar}), 8.04 (s, 4H, H_{Ar}), 8.03 (s, 4H, H_{Ar}), 2.58 (t, *J* = 6.8 Hz, 4H, H_{CPDIPS}), 2.27 – 2.19 (m, 4H, H_{CPDIPS}), 1.53 – 0.74 (m, 616H, $H_{CPDIPS/Hex}$) ppm.

MALDI-ToF *m/z* 7098 (calculated for $[C_{446}H_{720}N_{18}Si_{18}Zn_4]^+$: 7101.8).

UV-vis-NIR (toluene) λ_{max} (log ε): 794 (5.16), 493 (5.54), 430 (5.36).

Synthesis of *l*-P13

Scheme S3 depicts the synthetic route followed for the preparation of ***l*-P13**. Trimer **5** and pentamer **8** were prepared as reported previously.[1,2]

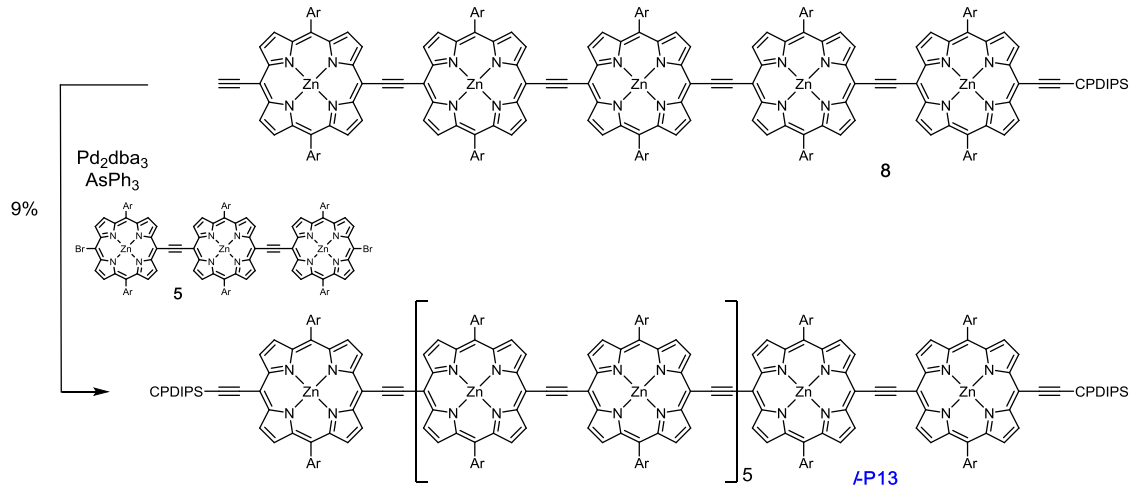

Scheme S3. Synthetic route for ***l*-P13**. Ar = 3,5-bis(trihexylsilyl)phenyl. CPDIPS = cyanopropyl-diisopropyl-silyl.

Porphyrin tridecamer ***l*-P13**:

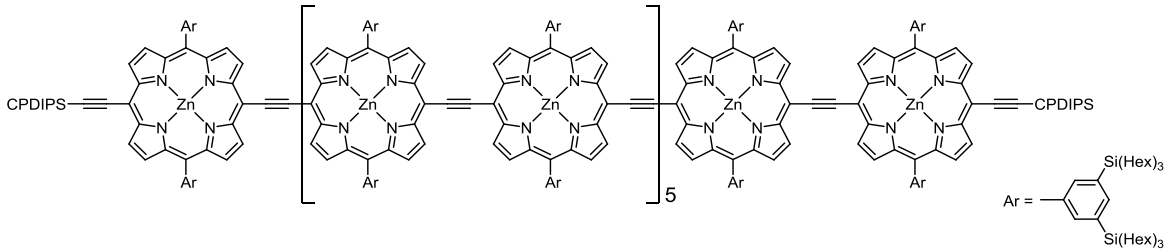

To a dried, argon flushed Schlenk-tube was added **5** (121 mg, 23 µmol) and **8** (175 mg, 20 µmol) together with dry THF (20 mL) and dry NEt_3 (2.5 mL) before performing two consecutive freeze-pump-thaw cycles. While frozen, $Pd_2(dba)_3$ (3.7 mg, 4 µmol) and $AsPh_3$ (8.9 mg, 29 µmol) were added under a stream of argon, before performing three additional freeze-pump-thaw cycles. The solution was heated to 50 °C for 2 d before cooling to room temperature and removing the solvents under reduced pressure. A short plug (NEt_3-deactivated SiO_2; $PE_{40–60}/CH_2Cl_2$ 1:1), and subsequent short SEC (toluene + 1% pyridine) and recycling GPC (toluene + 1% pyridine) yielded ***l*-P13** (20.1 mg, 9%) as a dark brown oily solid.

^{1}H NMR (400 MHz, $CDCl_3$, 298 K): δ_H 10.43 – 10.37 (m, 48H, H_β), 9.72 (d, J = 4.4 Hz, 4H, H_β), 9.13 – 9.07 (m, 48H, H_β), 8.95 (d, J = 4.4 Hz, 4H, H_β), 8.42 – 8.32 (m, 52H, H_{Ar}), 8.06 – 8.03 (m, 26H, H_{Ar}), 2.81 (t, J = 4.8 Hz, 4H, H_{CPDIPS}), 2.27 – 2.19 (m, 4H, H_{CPDIPS}), 1.57 – 0.72 (m, 2060H, $H_{CPDIPS/Hex}$) ppm.

MALDI-ToF *m/z* 22216 (calculated for $[C_{1400}H_{2250}N_{54}Si_{54}Zn_{13}]^+$: 22206).

UV-vis-NIR (toluene) λ_{max} (log ε): 833 (5.70), 496 (6.03), 433 (5.76).

^{1}H NMR spectra of new compounds

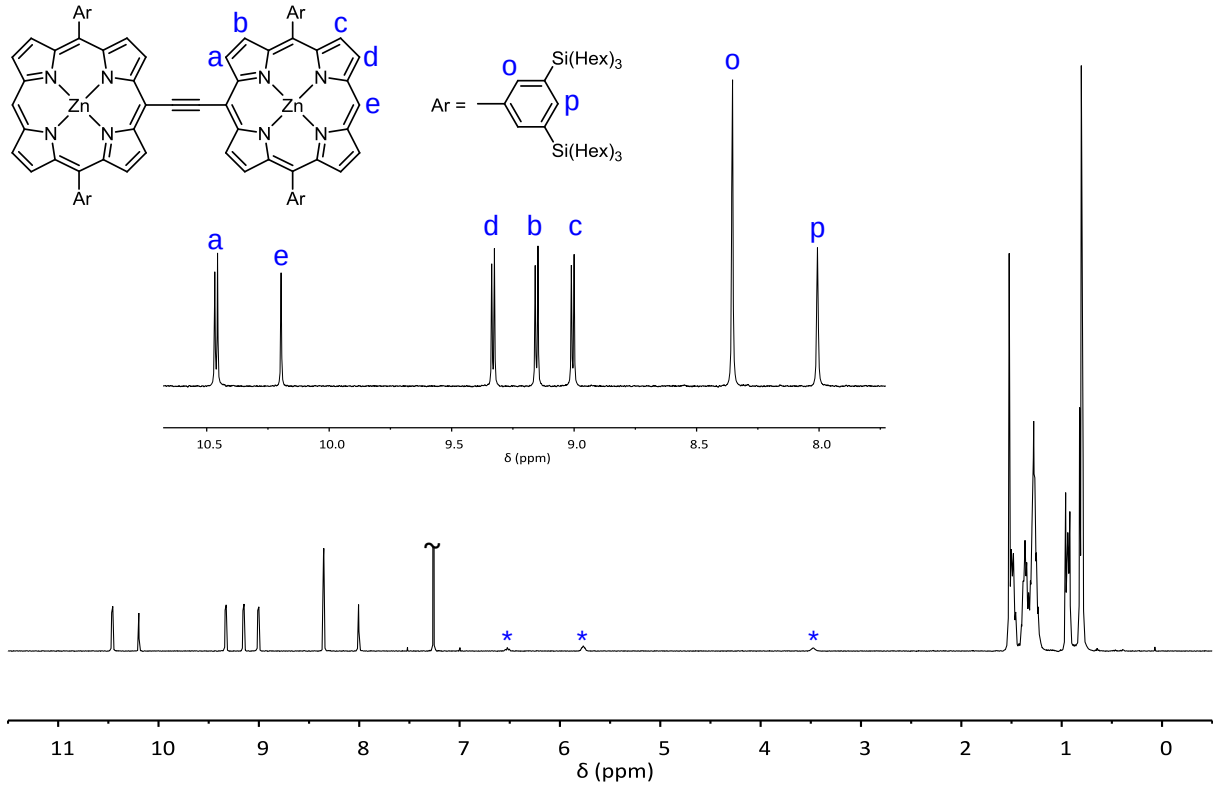

Figure S1. ^{1}H NMR spectrum of compound **3** (400 MHz, $CDCl_3$, 298 K, * denotes coordinated pyridine).

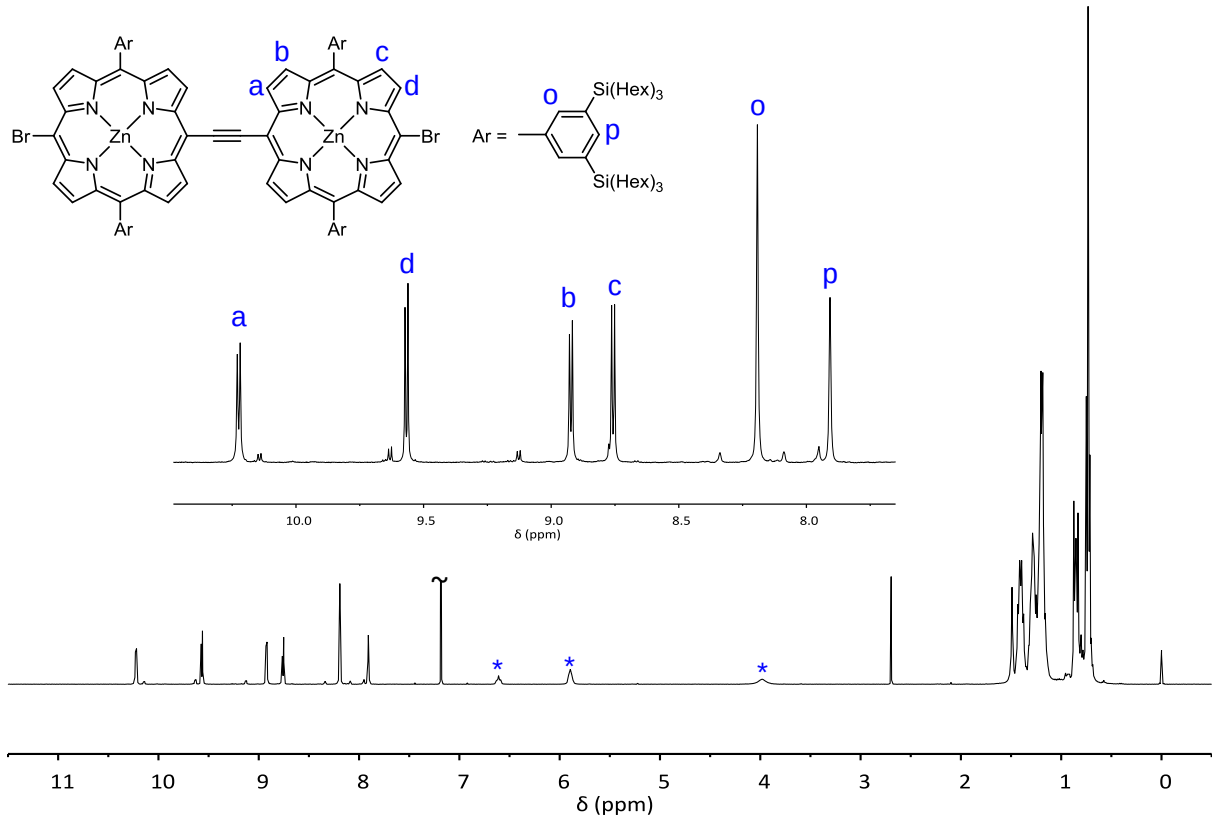

Figure S2. ^{1}H NMR spectrum of compound **4** (400 MHz, $CDCl_3$, 298 K, * denotes coordinated pyridine).

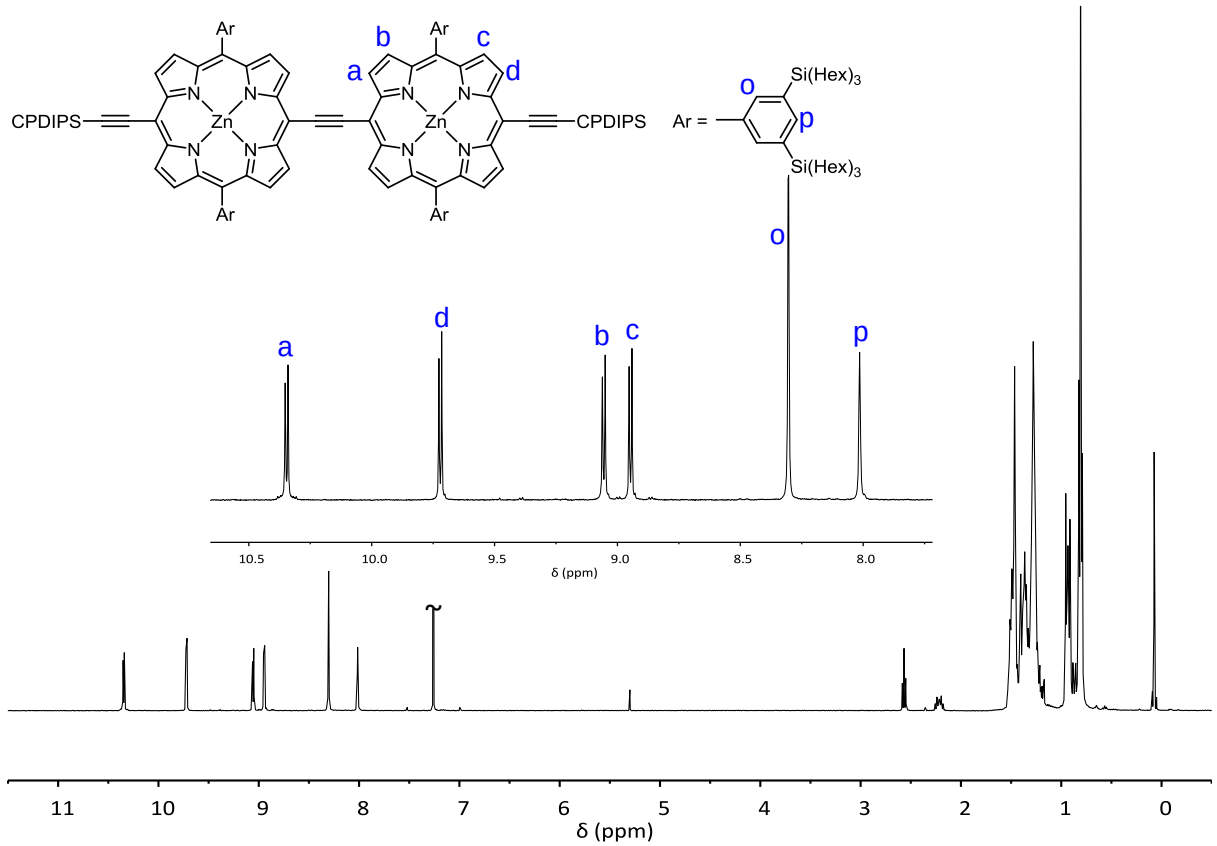

Figure S3. ^{1}H NMR spectrum of compound ***l*-P2** (400 MHz, $CDCl_3$, 298 K).

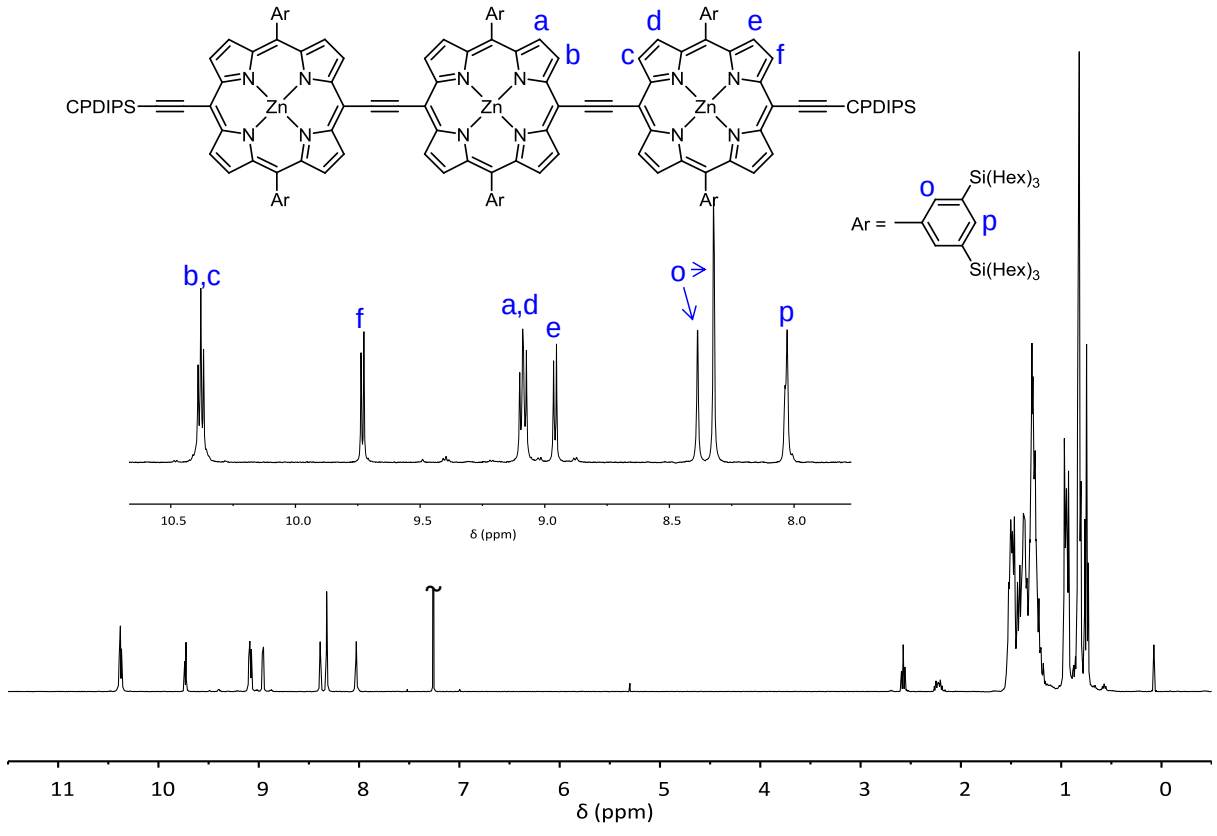

Figure S4. ^{1}H NMR spectrum of compound ***l*-P3** (400 MHz, $CDCl_3$, 298 K).

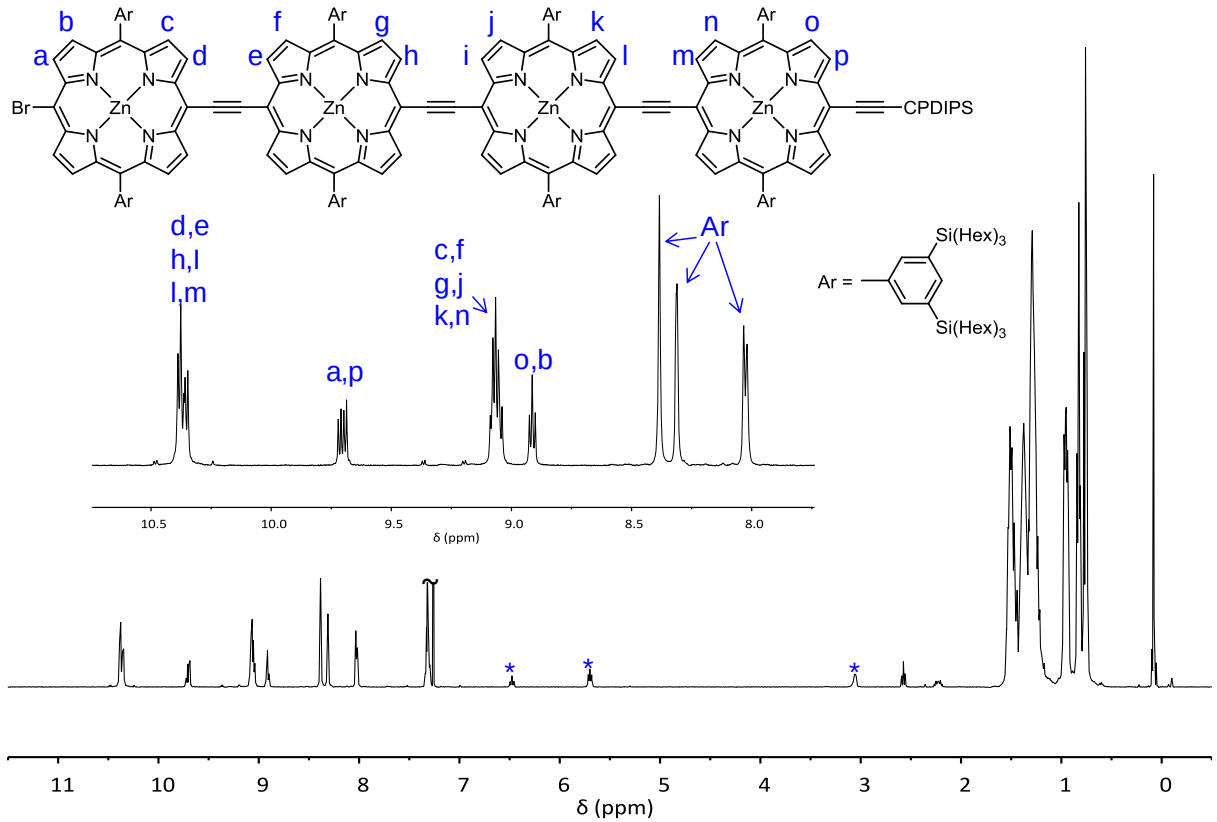

Figure S5. ^{1}H NMR spectrum of compound **7** (400 MHz, $CDCl_3$, 298 K, * denotes coordinated pyridine).

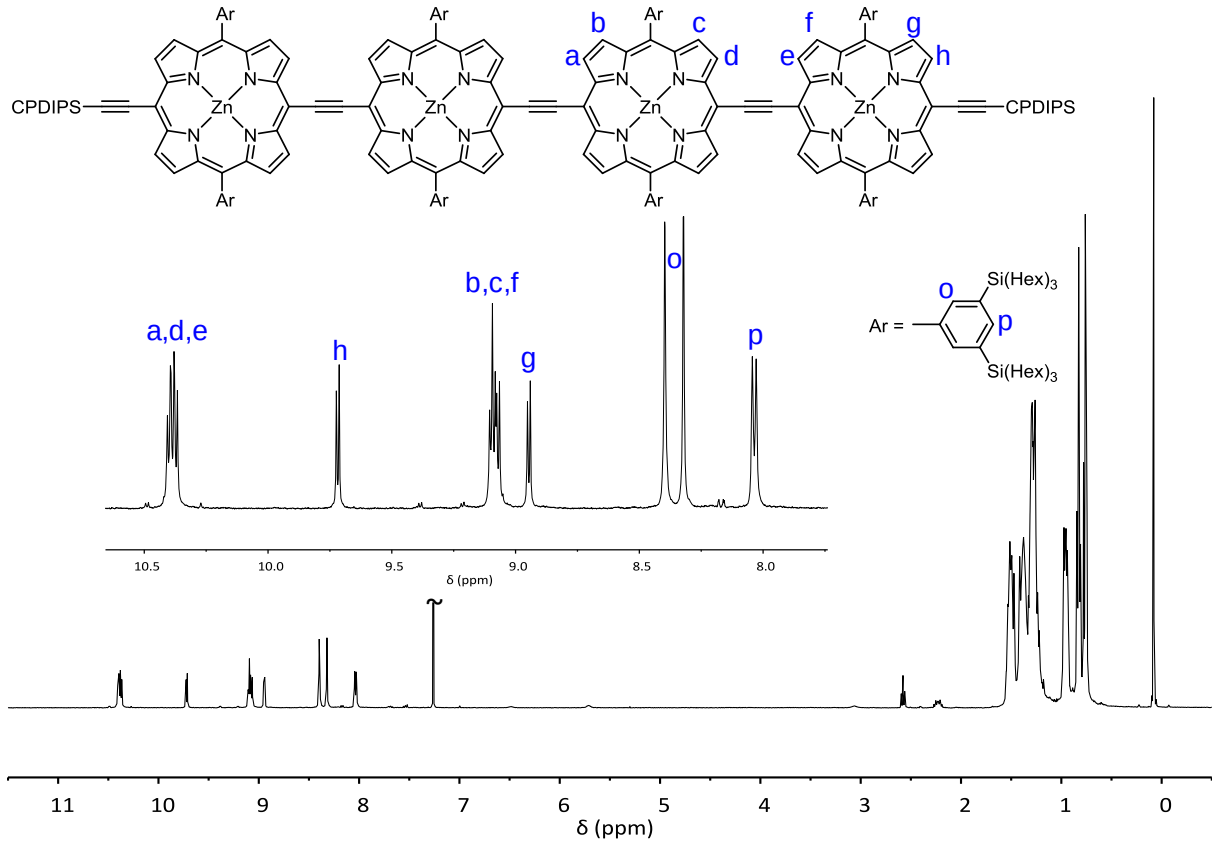

Figure S6. ^{1}H NMR spectrum of compound ***l*-P4** (400 MHz, $CDCl_3$, 298 K).

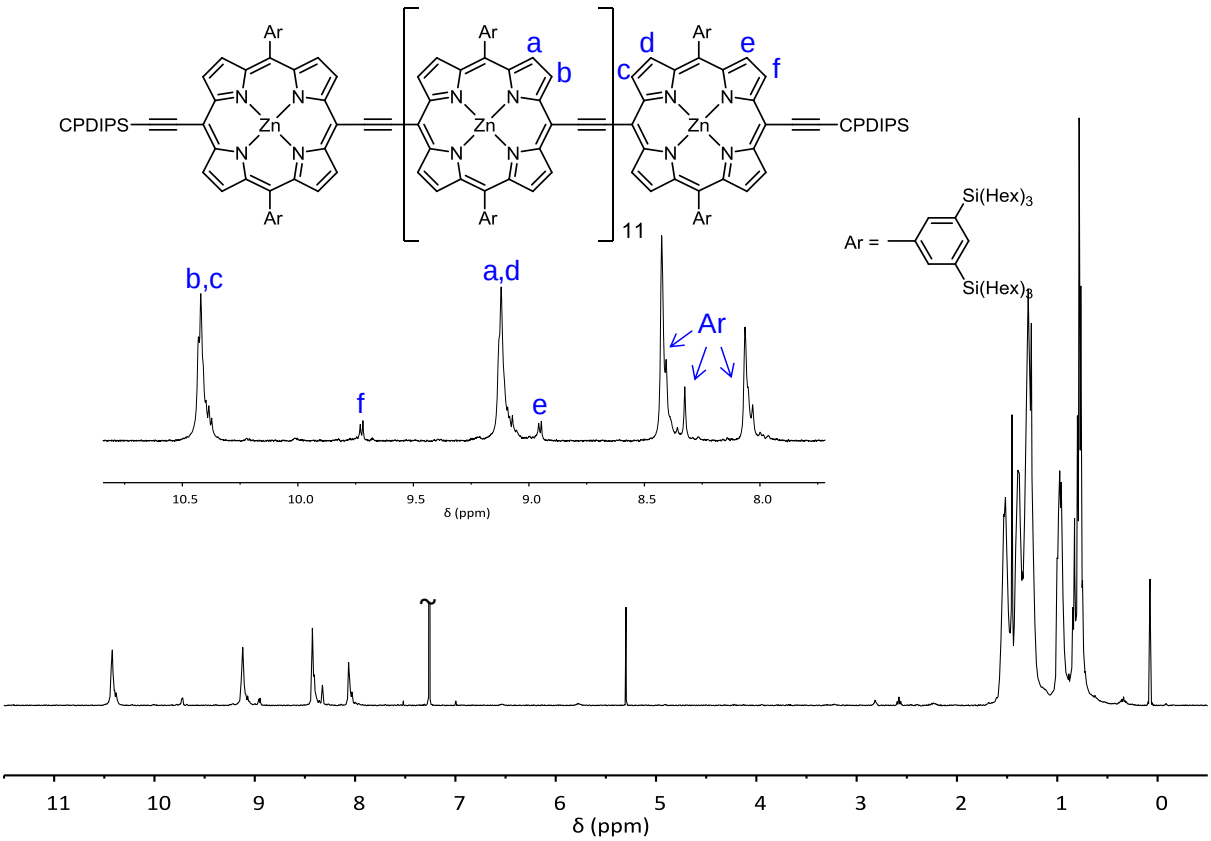

Figure S7. ^{1}H NMR spectrum of compound ***l*-P13** (400 MHz, $CDCl_3$, 298 K).

Equation 1 (The Norris Equation)

Continuous-wave EPR spectra of porphyrin radical cations such as the ones investigated in this work are typically analyzed based on a theoretical relationship between the EPR spectral linewidth and the oligomer chain length established in 1971 by Norris *et al.* and verified experimentally in the same work.[4] Although not explicitly demonstrated in the original work, the origin of this relationship (referred to as Equation 1) can be traced back to the properties of multinomial coefficients. Furthermore, as will be illustrated, the true value of Equation 1 comes from the fact that, in the limit of large numbers of nuclei, the binomial distribution approximates a Gaussian distribution. This section is concerned with the derivation of Equation 1 for stick spectra and a discussion of the potential pitfalls of using arguments based solely on linewidth considerations.

N spin-½ nuclei

The derivation starts by writing the ESR spectrum of an electron spin coupled to N equivalent spin-½ nuclei in analytical form as:

$$S_N(B) = \sum_{k=-N/2}^{+N/2} \frac{1}{2^N} C^N_{k+\frac{N}{2}} \delta(B + 2kA_N)$$

The above expression describes an EPR spectrum (Figure S8) in field domain, $S(B)$, comprised of $(N+1)$ equidistant infinitesimally thin lines separated by the hyperfine coupling constant, $2A_N$ (hence the use of the Dirac delta function). The intensity of each line is given by the binomial coefficient, $C^N_{k+\frac{N}{2}}$, and the factor of $1/2^N$ ensures that the spectrum is normalized to the integral:

$$\int_{-\infty}^{+\infty} S_N(B)dB = \frac{1}{2^N} \sum_{k=-N/2}^{+N/2} C^N_{k+\frac{N}{2}} = 1$$

Note that, as written, this spectrum has a center field of zero, which means that the real field axis is obtained by shifting to an appropriate center field ($B_{\mathrm{real}} = B + B_{\mathrm{centre}}$).

The variance of the spectrum relative to $B = 0$ is defined as:

$$\Delta B_N^2 = \int_{-\infty}^{+\infty} B^2 S_N(B)dB = \frac{1}{2^N} \sum_{k=-\frac{N}{2}}^{+\frac{N}{2}} C^N_{k+\frac{N}{2}} (2kA_N)^2$$

If we now assume that the hyperfine coupling to each one of the N nuclei is given by $A_N = A_1/N$, the equation for ΔB_N^2 becomes:

$$\Delta B_N^2 = \frac{A_1^2}{N^2 2^{N-2}} \sum_{k=-\frac{N}{2}}^{+\frac{N}{2}} k^2 C^N_{k+\frac{N}{2}}$$

The sum of binomial coefficients can be trivially evaluated either by using the factorization properties of the binomial coefficients or by twice differentiating $(1+x)^N$ with respect to x and setting $x = 1$, to yield:

$$\sum_{k=-\frac{N}{2}}^{+\frac{N}{2}} k^2 C^N_{k+\frac{N}{2}} = N2^{N-2}$$

By substituting the above relation into the final expression for the second moment, we obtain:

$$\Delta B_N^2 = \frac{A_1^2}{N}$$

And because $\Delta B_1^2 = A_1^2$, this is simply the square of Equation 1 in the main text.

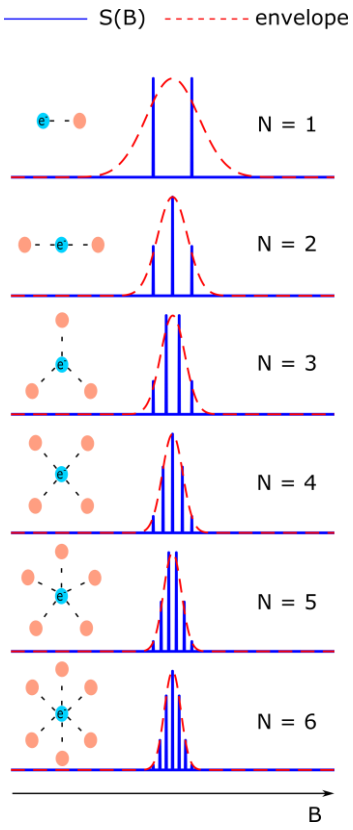

Figure S8. Stick spectra for an electron spin coupled to $N = 1 - 6$ equivalent spin-1/2 nuclei with a hyperfine coupling constant which is inversely proportional the number of nuclei ($A_N = A_1/N$, where A_1 is the hyperfine coupling in the $N = 1$ case). The red dotted line shows the Gaussian envelope of the spectra obtained from least-squares fitting to the stick spectra. As N becomes larger, the Gaussian scaling of the spectra becomes clearer.

N spin-1 nuclei

Since porphyrin molecules also contain ^{14}N nuclei, it is necessary to consider the second moment of the EPR spectra resulting from a coupling to N spin-1 nuclei, i.e.:

$$S_N(B) = \frac{1}{3^N} \sum_{k=-N}^{+N} T_k^N \delta(B + kA_N)$$

where T_k^N is a trinomial coefficient contained in the expansion of $(1 + x + x^{-1})^N$. The spectrum consists of $(2N + 1)$ infinitesimally thin lines centered around zero and separated

by A_N with an intensity given by T_k^N. Once again, the factor of $1/3^N$ ensures the spectrum is normalized to a unit integral.

The second moment of this spectrum can be written similarly to the spin-1/2 case as:

$$\Delta B_N^2 = \frac{A_1^2}{N^2 3^N} \sum_{k=-N}^{+N} k^2 T_k^N$$

The summation over the trinomial coefficients can be evaluated separately[1]:

$$\sum_{k=-N}^{+N} k^2 T_k^N = 2N3^{N-1}$$

And thus, we obtain:

$$\Delta B_N^2 = \frac{2A_1^2}{3N}$$

As before, this is Equation 1 and it is valid for couplings to N equivalent spin-1 nuclei.

N spin-1 nuclei and *M* spin-½ nuclei

By combining the expressions for the spectra in the two cases discussed above, we can construct the expression for the ESR spectrum in the case when an electron is coupled to N equivalent spin-1 nuclei and M equivalent spin-½ nuclei:

$$S_{NM}(B) = \frac{1}{3^N} \sum_{k=-N}^{+N} T_k^N \mathcal{S}_M(B + kA_N) = \frac{1}{3^N} \frac{1}{2^M} \sum_{k=-N}^{+N} T_k^N \sum_{j=-M/2}^{+M/2} C_{j+\frac{M}{2}}^M \delta(B + kA_N + 2j\mathcal{A}_M)$$

Where $A_N = A_1/N$ and $\mathcal{A}_M = \mathcal{A}_1/M$ are the hyperfine couplings to the spin-1 and spin-½ nuclei, respectively.

The second moment of $S_{NM}(B)$ is thus written as:

$$\Delta B_{NM}^2 = \frac{1}{3^N} \sum_{k=-N}^{+N} T_k^N \int_{-\infty}^{+\infty} B^2 \mathcal{S}_M(B + kA_N) dB$$

The integral in the expression above can be evaluated by first changing variables and expanding the square:

$$\int_{-\infty}^{+\infty} B^2 \mathcal{S}_M(B + kA_N) dB = \int_{-\infty}^{+\infty} (B - kA_N)^2 \mathcal{S}_M(B) dB =$$

$$= \int_{-\infty}^{+\infty} B^2 \mathcal{S}_M(B) dB - 2kA_N \int_{-\infty}^{+\infty} B\mathcal{S}_M(B) dB + k^2 A_N^2 \int_{-\infty}^{+\infty} \mathcal{S}_M(B) dB =$$

$$= \frac{\mathcal{A}_1^2}{M} + \frac{k^2 A_1^2}{N^2}$$

Substituting this result into the expression for ΔB_{NM}^2 and evaluating the sums individually:

[1] By differentiating $(1 + x + x^{-1})^N$ twice at $x = 1$.

$$\Delta B_{NM}^2 = \frac{1}{3^N}\sum_{k=-N}^{+N} T_k^N \left(\frac{\mathcal{A}_1^2}{M} + \frac{k^2 A_1^2}{N^2}\right) = \frac{\mathcal{A}_1^2}{M} + \frac{2A_1^2}{3N}$$

The above is the most general expression for the variance of the ESR spectrum of an electron coupled to N equivalent spin-1 nuclei and M equivalent spin-½ nuclei. For example, in a porphyrin monomer, such as ***I*-P1$^{+\bullet}$**, we have $N = M = 4$ and $\mathcal{A}_1 \approx 1$ MHz and $A_1 \approx 4.3$ MHz for proton and nitrogen nuclei, respectively. In the case of complete and uniform delocalization an oligomer would contain nN spin-1 nuclei and nM spin-½ nuclei where n is the oligomer chain length, and the second moment becomes:

$$\Delta B_{(nN)(nM)}^2 = \frac{1}{n}\left(\frac{\mathcal{A}_1^2}{M} + \frac{2A_1^2}{3N}\right) = \frac{\Delta B_{NM}^2}{n}$$

After adjusting the notation, this is just the square of Equation 1 in the main text:

$$\Delta B_N = \frac{\Delta B_1}{\sqrt{N}}$$

Where N is now the oligomer chain length, and ΔB_1 is the second moment of the monomer spectrum.

Limit of large numbers of nuclei

The problem with evaluating the second-moment of real ESR spectra is that they are not formed of infinitely thin lines; the peaks have an inherent linewidth. This means that the expressions for ΔB_N in the above derivations do not simplify to finite sums, and the integral:

$$\Delta B_N^2 = \int_{-\infty}^{+\infty} B^2 S_N(B) dB$$

has to be evaluated numerically. This numerical integral evaluation together with the fact that the ESR spectra are recorded as the 1st Harmonic of $S_N(B)$ and that there is an uncertainty in determining the center field of the integration range means that a direct evaluation of the second-moment from the integral is prone to many (unquantifiable) error sources.

However, the stick spectra discussed above have a Gaussian scaling property (in the limit of large numbers of nuclei; see Figure S8) which enables a different, and much more accurate, approach to be taken in evaluating the second-moment. We will first illustrate the Gaussian scaling property for the case of many equivalent spin-½ nuclei. Starting from the general expression for the spectrum, as written before:

$$S_N(B) = \sum_{k=-N/2}^{+N/2} \frac{1}{2^N} C_{k+\frac{N}{2}}^N \delta(B + 2kA_N)$$

To proceed, we make use of the following two scaling relationships[2]:

$$\lim_{N\to\infty} \sum_{k=-N/2}^{N/2} f(k) \sim \int_{-\infty}^{+\infty} f(k) dk$$

[2] The second scaling relationship is derived by using (the exponentiated form of) Stirling's approximation.

$$\lim_{N\to\infty}\frac{1}{2^N}C^N_{k+\frac{N}{2}} \sim \frac{2}{\sqrt{2\pi N}}e^{-2k^2/N}$$

to re-write the equation for the spectrum as:

$$S_N(B) \sim \int_{-\infty}^{+\infty}\frac{2}{\sqrt{2\pi N}}e^{-2k^2/N}\delta(B+2kA_N)dk =$$

$$= \int_{-\infty}^{+\infty}\frac{2}{\sqrt{2\pi N(2A_N)^2}}e^{-2k^2/N}\delta(B+2kA_N)d(2kA_N)$$

Evaluating the 'sifter' integral above leads to the following first order scaling relationship for $S(B)$ when the number of nuclei is large:

$$S(B) \sim \frac{2}{\sqrt{2\pi N(2A_N)^2}}e^{-2B^2/4NA^2}$$

This equation implies that the envelope of the spectrum becomes an ever better approximation of a Gaussian distribution with variance:

$$\Delta B_N^2 = NA_N^2$$

If the spin density is distributed equally amongst the N nuclei then we can use $A_N = A_1/N$ to obtain:

$$\Delta B_N^2 = \frac{A_1^2}{N} \xRightarrow{\text{re-write}} \Delta B_N = \frac{\Delta B_1}{\sqrt{N}}$$

The above equation confirms that Equation 1 of the main text is readily generalized to large numbers of nuclei. Furthermore, the derivation can further be shown to apply for spin-1 nuclei and for combinations of different types of nuclei. Whilst this result is not at all surprising (the previous result is completely general i.e. even if N is large), it is far reaching. It implies that if the number of nuclei in the porphyrin oligomers of interest in this work is large (and it is) then the spectra should have a strictly Gaussian envelope (and they do) with a width that obeys Equation 1. As a result, fitting a Gaussian to the experimental spectra is a valid method for obtaining the second moment of the spectrum. However, there are a few relevant caveats which follow from the above derivation:

- If the number of nuclei is not large enough then the envelope of the spectrum will deviate more significantly from a Gaussian function. This is, in fact, observed in the spectrum of the porphyrin monomer (see main text and the next sections) where the best fit envelope of the monomer has a larger uncertainty.
- If the lines have a finite but small Lorentzian linewidth then, we expect the spectrum for the larger oligomers to scale more as a Lorentzian because it is essentially only a superposition of Lorentzians with small separations between the centers. As a result, we do not expect Equation 1 to be applicable if the largest hyperfine coupling in the oligomer is smaller than the inherent Lorentzian linewidth. This effect is observed in the spectrum of ***I*-P13$^{+\bullet}$** (shown in the next Section) whose envelope is significantly better represented by a Lorentzian function (cf. Figure S9 and Figure S10). Nonetheless, as far as the variance (or the second-moment) of the spectra investigated in this work is concerned, both Gaussians and Lorentzians give rise to the same deviation from Equation 1.

- If the assumption of complete and uniform delocalization is not entirely followed, *i.e.* if $A_N \neq A_1/N$, then the critical last step in *all* the derivations above is invalid, and Equation 1 will not be obeyed. However, we can show that the Gaussian scaling remains valid. Some particular aspects of this case are considered in more detail in the next section.

First-order generalization of Equation 1

Consider a simplified EPR spectrum of a monomeric porphyrin radical cation in which we neglect the hyperfine couplings to the protons and only consider the hyperfine couplings, a, to the equivalent nitrogen nuclei. In this case, we can write the analytical spectrum as:

$$S_1(B) = \frac{1}{3^N} \sum_{k=-N}^{+N} T_k^N \delta(B + ka)$$

Where $N = 4$ in the specific case considered here, but the derivation will be shown for (almost) any integer N. The second moment of $S_1(B)$ is:[3]

$$\Delta B_1^2 = \frac{2Na^2}{3}$$

We can now construct the dimer spectrum in the case of non-uniform delocalization by defining a *non-uniformity parameter*, q, such that N nuclei have an enhanced hyperfine coupling $\left(\frac{a}{2} + qa\right)$ and the remaining N nuclei have a reduced hyperfine coupling $\left(\frac{a}{2} - qa\right)$. We can see that $q = 0$ corresponds to complete and uniform delocalization. Moreover, we see that the sum of the hyperfine couplings on all the nuclei is equal to the sum of the hyperfine couplings in the monomer, i.e. the spin density is normalized to the monomer. If $q \neq 0$ then we can see in Figure S9 that there are different indistinguishable patterns for distributing the spin density relative to the structure of the dimer. In any case, the dimer spectrum can thus be written as:

$$S_2(B) = \frac{1}{3^N} \sum_{k=-N}^{+N} T_k^N \mathcal{S}\left(B + k\left(\frac{a}{2} + qa\right)\right)$$

$$= \frac{1}{3^{2N}} \sum_{k=-N}^{+N} T_k^N \sum_{j=-N}^{+N} T_k^N \ \delta\left(B + k\left(\frac{a}{2} + qa\right) + j\left(\frac{a}{2} - qa\right)\right)$$

[3] Using the relation shown in the general spin-1 case from before.

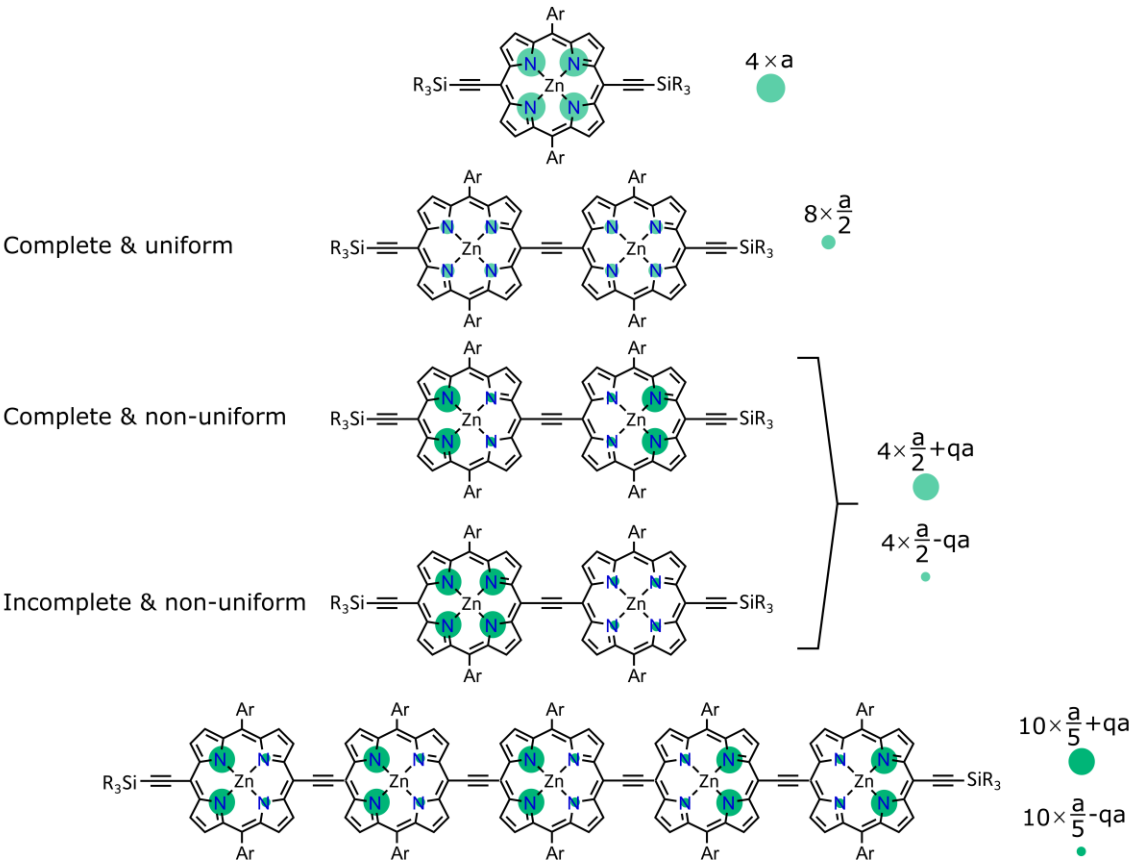

Figure S9. Illustration of the non-uniformity parameter, $\boldsymbol{q}$, as applicable to the nitrogen hyperfine couplings within the series of linear porphyrin oligomers relevant for this work. In the case of the dimer, $\boldsymbol{q} = \mathbf{0}$ corresponds to 8 equivalent ^{14}N hyperfine couplings of magnitude $\boldsymbol{a/2}$ i.e. complete and uniform delocalization of the spin density. When $\boldsymbol{q} \neq \mathbf{0}$, we can distinguish multiple cases, two of which are illustrated here. The most surprising case is the complete but non-uniform distribution: each porphyrin unit has 50% of the spin density, i.e. complete delocalization, however, the central and peripheral ^{14}N nuclei are inequivalent and as a result, Equation 1 is not applicable.

And we see that if $q = 0$, the expression reduces to the usual dimer spectrum equation. In the case of a general oligomer with a chain length p we can also define, by analogy with the dimer, a non-uniformity parameter, q, such that $\frac{pN}{2}$ nuclei have couplings $\left(\frac{a}{p} \pm qa\right)$.[4] The non-uniformity parameter is exemplified visually by reference to the pentamer structure in Figure S9. The ESR spectrum in the general case is therefore given by:

$$S_p(B) = \frac{1}{3^{pN/2}} \sum_{k=-pN/2}^{+pN/2} T_k^{pN/2} \mathcal{S}\left(B + k\left(\frac{a}{p} + qa\right)\right)$$

$$= \frac{1}{3^{pN/2}} \sum_{k=-pN/2}^{+pN/2} T_k^{pN/2} \sum_{j=-pN/2}^{+pN/2} T_k^{pN/2}\ \delta\left(B + k\left(\frac{a}{p} + qa\right) + j\left(\frac{a}{p} - qa\right)\right)$$

[4] This derivation only works **either** *for even numbers of nuclei in the monomer* **or** *even chain lengths* which is sufficient for porphyrin oligomers.

As before, we now evaluate the second moment of $S_p(B)$:

$$\Delta B_p^2 = \frac{1}{3^{pN/2}} \sum_{k=-pN/2}^{+pN/2} T_k^{pN/2} \int_{-\infty}^{+\infty} B^2 \mathcal{S}\left(B + k\left(\frac{a}{p} + qa\right)\right) dB$$

The integral is evaluated by changing variables and expanding the square:

$$\begin{aligned}
\int_{-\infty}^{+\infty} B^2 \mathcal{S}\left(B + k\left(\frac{a}{p} + qa\right)\right) dB &= \int_{-\infty}^{+\infty} \left(B - k\left(\frac{a}{p} + qa\right)\right)^2 \mathcal{S}(B) dB \\
&= \int_{-\infty}^{+\infty} B^2 \mathcal{S}(B) dB - 2k\left(\frac{a}{p} + qa\right) \int_{-\infty}^{+\infty} B\mathcal{S}(B) dB + k^2 \left(\frac{a}{p} + qa\right)^2 \int_{-\infty}^{+\infty} \mathcal{S}(B) dB \\
&= \frac{pN}{3}\left(\frac{a}{p} - qa\right)^2 + k^2 \left(\frac{a}{p} + qa\right)^2
\end{aligned}$$

Therefore, we have the second moment of the p-th oligomer spectrum:

$$\Delta B_p^2 = \frac{pN}{3}\left(\frac{a}{p} - qa\right)^2 + \frac{pN}{3}\left(\frac{a}{p} + qa\right)^2$$

Which simplifies to the following expression:

$$\Delta B_p^2 = \frac{2pN}{3}\left(\frac{a^2}{p^2} + q^2 a^2\right) = \frac{\Delta B_1^2}{p}\left(1 + p^2 q^2\right)$$

And by taking the square root we obtain:

$$\Delta B_p = \sqrt{1 + p^2 q^2}\,\frac{\Delta B_1}{\sqrt{p}}\ ;\ \forall p > 1$$

This final equation is a first order generalization of Equation 1 of the main text which accounts for the fact that for $p > 1$ the spin density can be non-uniformly delocalized over the individual nuclei, as quantified by a single parameter, q. The applicability of this generalized equation compared to Equation 1 will be explored in the next section.

Continuous wave EPR

Acquisition parameters

The continuous wave (cw) X-band EPR spectra were acquired at room temperature on a Bruker EMX Micro spectrometer equipped with a high sensitivity Bruker probe head. The microwave frequency of operation was *ca.* 9.40 GHz and the spectra were acquired with a modulation amplitude of 0.01 mT and a modulation frequency of 100 kHz. This chosen modulation amplitude offered a compromise between the signal-to-noise ratio and the potential distortions caused by larger modulation amplitudes. The quality factor of the cavity was similar between all the measurements ($Q \approx 1000$). The microwave power was scanned to rule out linewidth distortions due to saturation effects. The optimal microwave power used in all the cw-EPR spectra in the main text was 2 mW corresponding to an attenuation of 20 dB on our spectrometer. The average spectra were obtained by combining individually recorded scans in order to ensure that the signal intensity remained constant in time.

Linewidth analysis

The experimental cw-EPR spectra were initially analyzed by fitting to the normalized data the first derivative of the following Gaussian function:

$$G(B) = \sqrt{\frac{2}{\pi}} \frac{1}{\Delta \mathrm{B_N}} e^{-2\left(\frac{B-B_0}{\Delta \mathrm{B_N}}\right)^2}$$

where B, B_0, and ΔB_N represent magnetic field, center field, and linewidth, respectively. The fitting was performed using the inbuilt MATLAB function *lsqnonlin* and the resulting values of ΔB_N were plotted against $1/\sqrt{N}$ in order to compare the results with Equation 1.

The 95% confidence interval relating to the envelope of the monomer spectrum (evaluated from the Jacobian matrix and residuals, as implemented in the *nlparci* function) is plotted as the dark grey shaded area in Figure S10. The gradient of the best-fit values of $\Delta B_{N\geq 2}$ was found to deviate significantly from the gradient predicted by Equation 1 even when an error of ±0.2 mT is considered on the monomer envelope (blue and light grey shaded areas in Figure S10). The envelope of the ***I*-P13$^{+\bullet}$** spectrum deviates significantly from a Gaussian function in line with the discussion in the previous section. This linewidth behavior for porphyrin oligomers with $N \geq 7$ was also observed in the work of Susumu *et al.*[5]

Secondly, the deviations from Equation 1 are also observed by considering the trend in the Lorentzian envelope linewidth, λ_N, obtained by fitting the derivative of the following function:

$$L(B) = \frac{2}{\pi\sqrt{3}} \frac{1}{\Delta \mathrm{B'}_N} \left[1 + \frac{4}{3}\left(\frac{B - B_0}{\Delta \mathrm{B'}_N}\right)^2\right]^{-1}$$

As can be seen in Figure S11, this Lorentzian line shape does not describe accurately the shape of the envelope of the EPR spectra of the oligomers with $N \leq 5$. However, the Lorentzian function is a significantly better representation of the ***I*-P13$^{+\bullet}$**spectrum. Both the Gaussian and the Lorentzian analysis methods yield the same trend in envelope linewidth.

The third analysis is based on the generalized version of Equation 1, as derived in the previous section. The experimental results as well as the theoretical plot for a non-uniformity parameter in the range of 15-20% are shown in Figure S12. This range for q seems to

contain the experimental Gaussian linewidths of all the data points. As will be seen in the next sections, DFT calculations enable the spin densities of the individual ^{14}N nuclei to be determined and as a result the EPR spectra can be simulated directly. Nonetheless, from DFT we can still estimate an average non-uniformity parameter of ~7.5% which is half the one predicted in Figure S12. This is, however, an acceptable error given that the generalized version of Equation 1 assumes the existence of one clearly defined non-uniformity parameter, which is identical for all the porphyrins of a given oligomer and also, it neglects the influence of the inherent linewidth of the peaks.

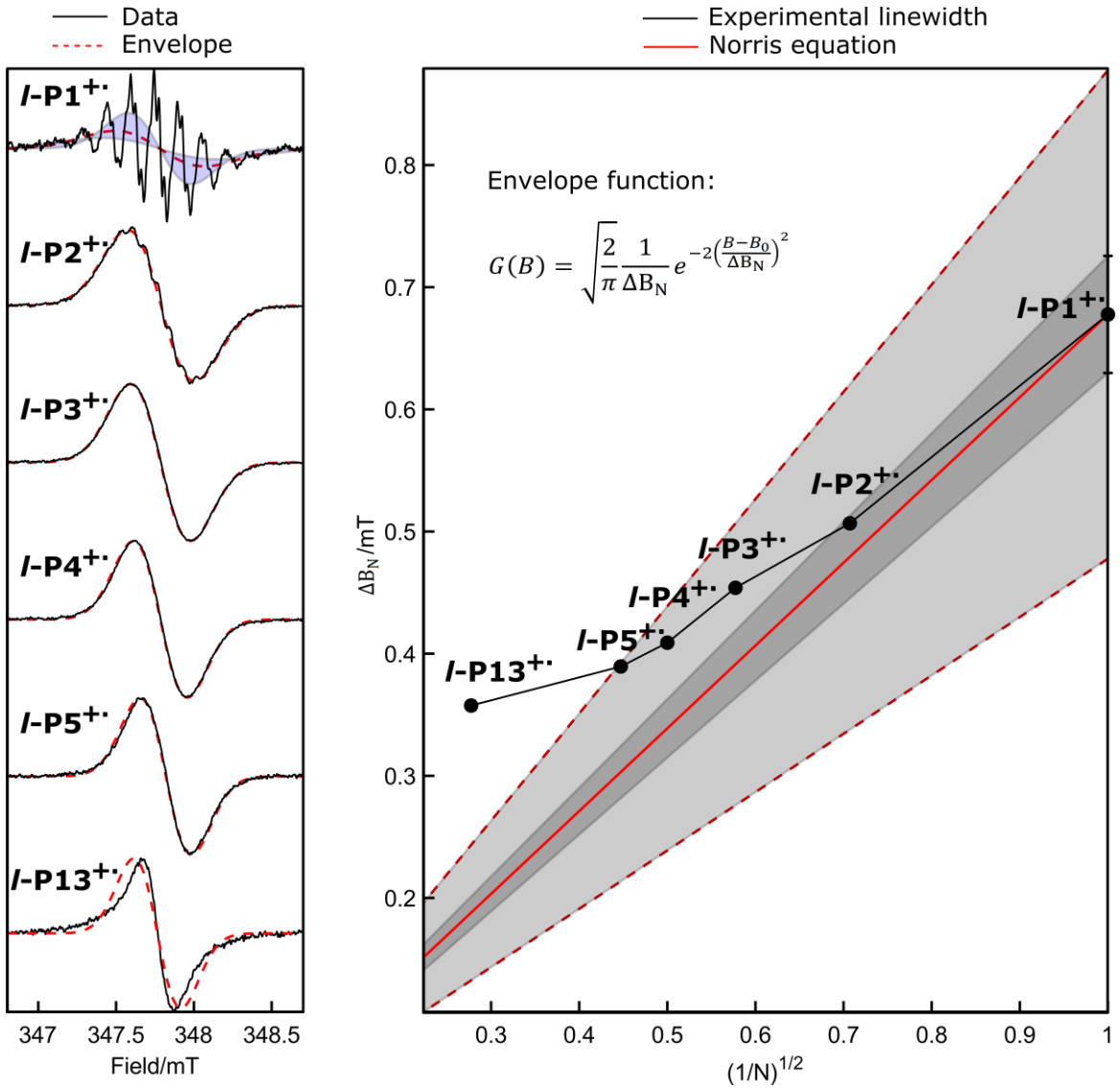

Figure S10. Linewidth analysis of the room temperature X-band cw-EPR spectra (black lines in the left panel) of the radical cations of the linear porphyrin oligomers using a derivative Gaussian function as a model for the spectral envelope (dashed red lines, left). The linewidth of the best fit Gaussian envelope is plotted against $\boldsymbol{N^{-0.5}}$ in the right panel (black circles). The dark grey shaded area represents the 95% confidence interval of the linewidth of the monomer spectrum, whereas the light grey shaded area shows an exaggerated uncertainty of $\pm$0.2 mT. The light grey shaded area in the right panel corresponds to the blue shaded area (enclosed by two Gaussians) in the left panel on top of the monomer spectrum. This exaggerated uncertainty illustrates the fact that the deviation from Equation 1 (red line in the right panel) is significant.

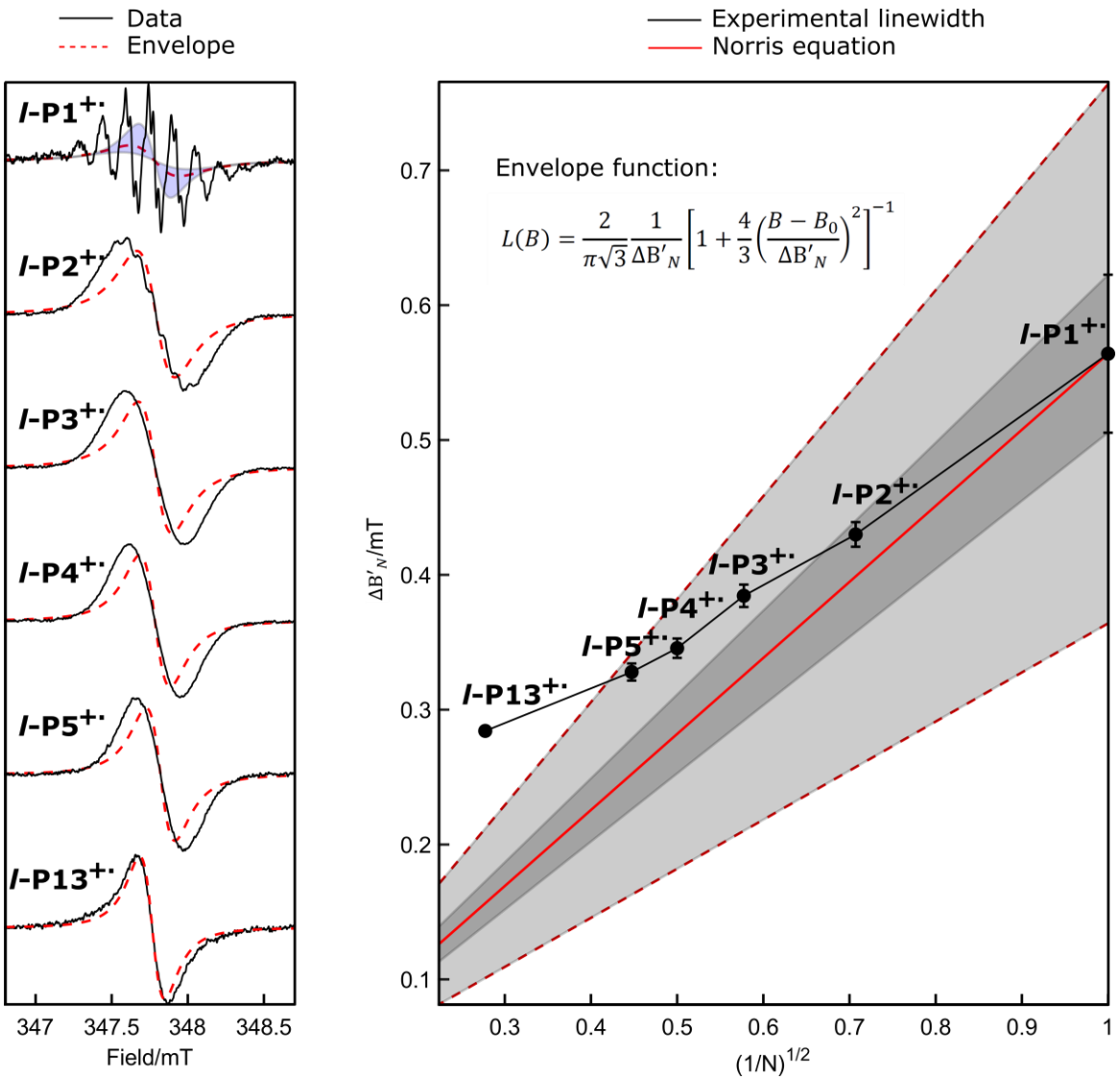

Figure S11. Linewidth analysis of the room-temperature X-band cw-EPR spectra of the radical cations of the linear porphyrin oligomers using a Lorentzian envelope function. See the caption to Figure S10 for details. The spectral envelope tends to a Lorentzian function as increasing the oligomer chain length.

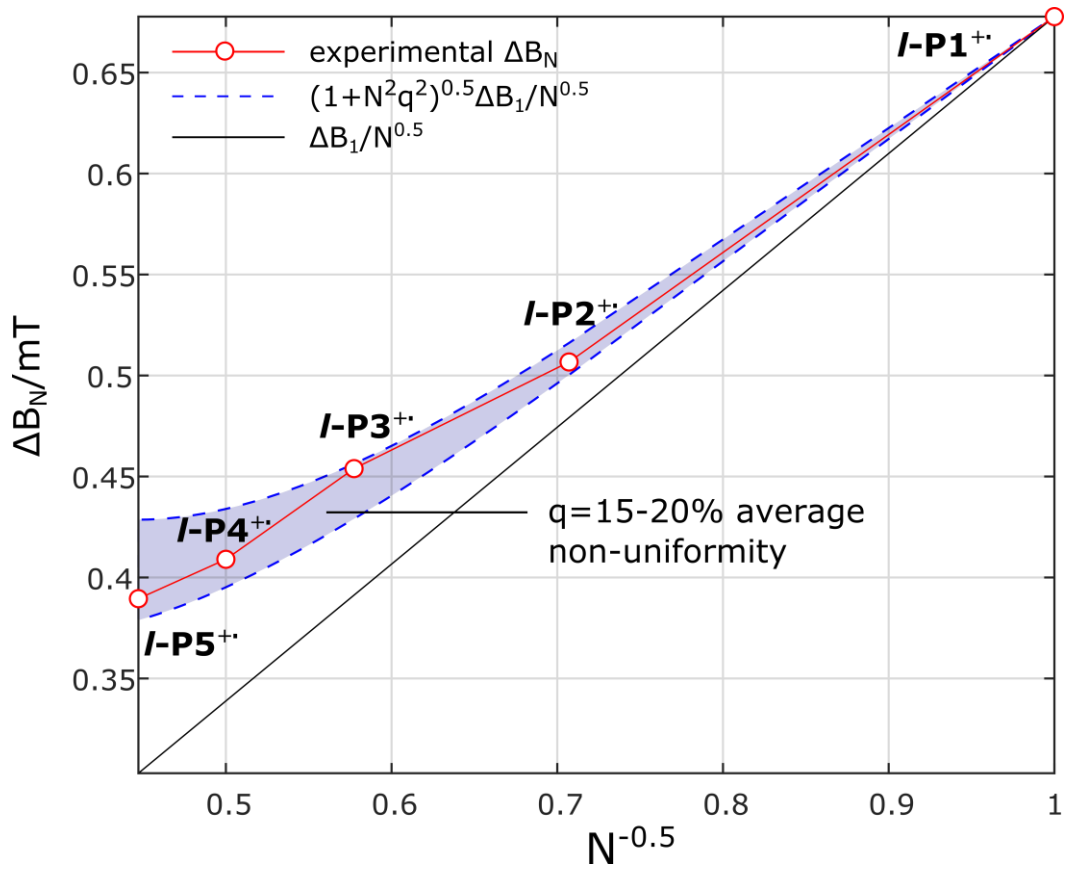

Figure S12. Linewidth analysis of the experimental Gaussian envelope linewidths for the linear oligomers ***l*-P1**$^{+\bullet}$ to ***l*-P1**$^{+\bullet}$ using the generalization of Equation 1, as derived in the previous subsection. The shaded area corresponds to a non-uniformity parameter, $\boldsymbol{q}$, in the range 15-20%.

Numerical simulations

The deviations from Equation 1 discussed in the main text and in the previous subsection are bound to be due to a failure of at least one of the assumptions which underpin its derivation. One of these essential assumptions is that the inherent linewidth of the EPR transitions is much smaller than the hyperfine coupling interaction (*i.e.* the line shape is hyperfine dominated and the individual peaks are separated by more than the width of the lines) or that this inherent linewidth remains constant (and small) for all the oligomers.

In order to assess the possible breakdown of this assumption, the EPR spectra were simulated using the function *garlic* implemented in EasySpin, a MATLAB package for EPR data simulation.[6,7] In the first instance, the best fit to the EPR spectrum of the porphyrin monomer was found by means of a least-squares fitting algorithm (in our case the Nedler-Mead simplex algorithm of the *esfit* function was used). The parameters optimized in this fitting are an isotropic hyperfine coupling, A_N, to 4 equivalent ^{14}N nuclei, an isotropic hyperfine coupling, A_H, to 4 equivalent ^{1}H nuclei, an isotropic g-value, and either a Lorentzian or a Gaussian inherent linewidth (simulations with a mixture of linewidths were also performed, however, the result of the optimization converged very closely to a predominant Lorentzian contribution). This particular choice of fitting parameters as well as their initial guess is based on the results of DFT calculations performed on the porphyrin monomer. The results of the DFT calculations (outlined in the next sections) are consistent with previous DFT and EPR studies on porphyrins with similar structures.[8,9]

After a suitable fit to the monomer spectrum is found, the spectra of the longer oligomers are obtained by dividing the values of A_N and A_H by the chain length, increasing the number of equivalent nuclei accordingly, and only allowing the inherent linewidth to be varied by the fitting algorithm. The results of these simulations are displayed in Figure S13 and Figure S14.

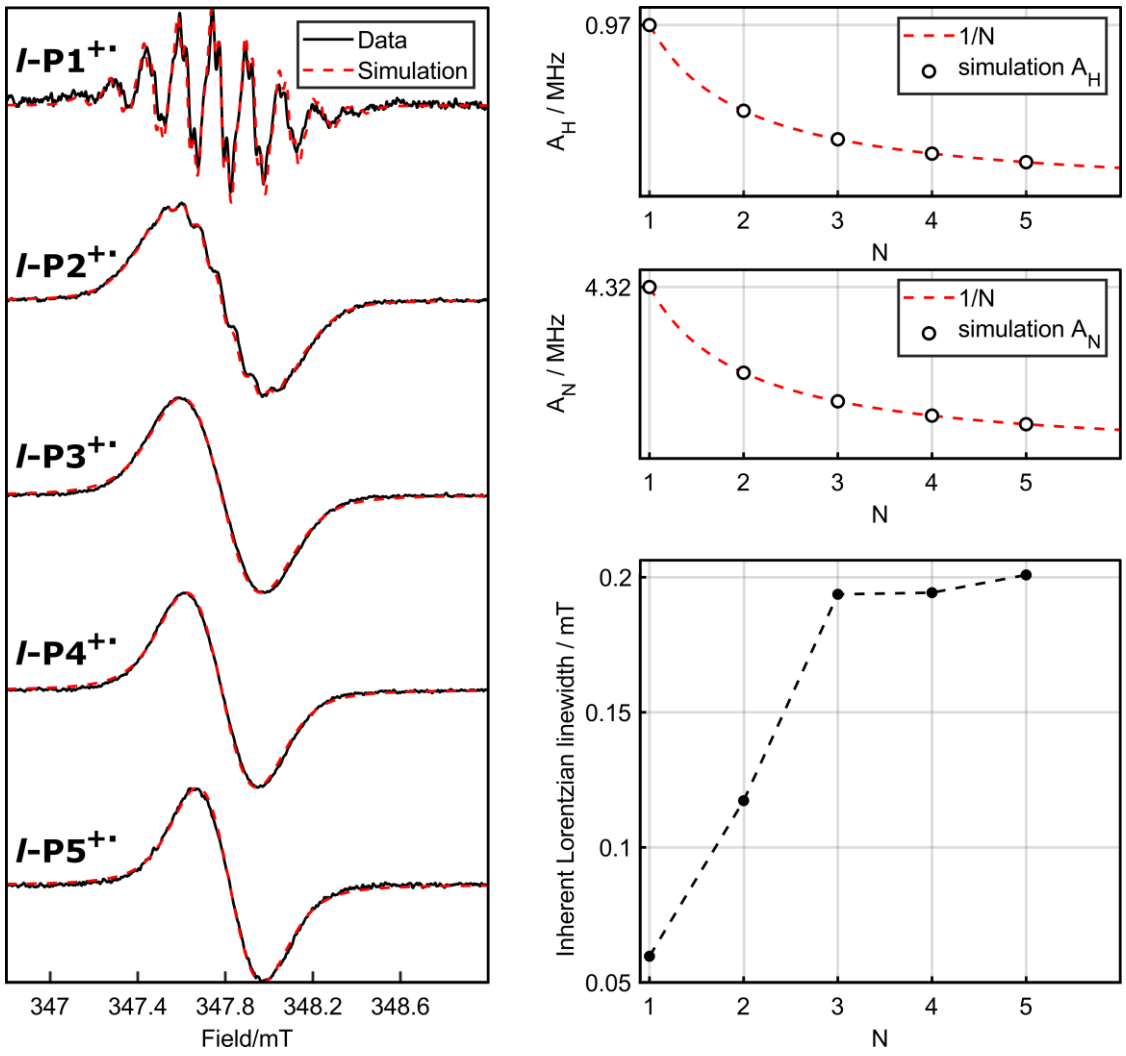

Figure S13. Numerical spectral simulations of the room temperature X-band cw-EPR spectra of the radical cations of the linear porphyrin oligomers up to ***l*-P5**$^{+\bullet}$ (the ***l*-P13**$^{+\bullet}$spectrum contains too many nuclei to allow a simulation using the current method). The best fit to the monomer spectrum was found using a three-parameter fitting of $\boldsymbol{A_H}$, $\boldsymbol{A_N}$ and an inherent Lorentzian linewidth. The simulations for the longer oligomers were obtained from a one-parameter fitting of the inherent linewidth, whilst the hyperfine couplings were divided by the oligomer chain length (*i.e.* uniform delocalization) and kept constant.

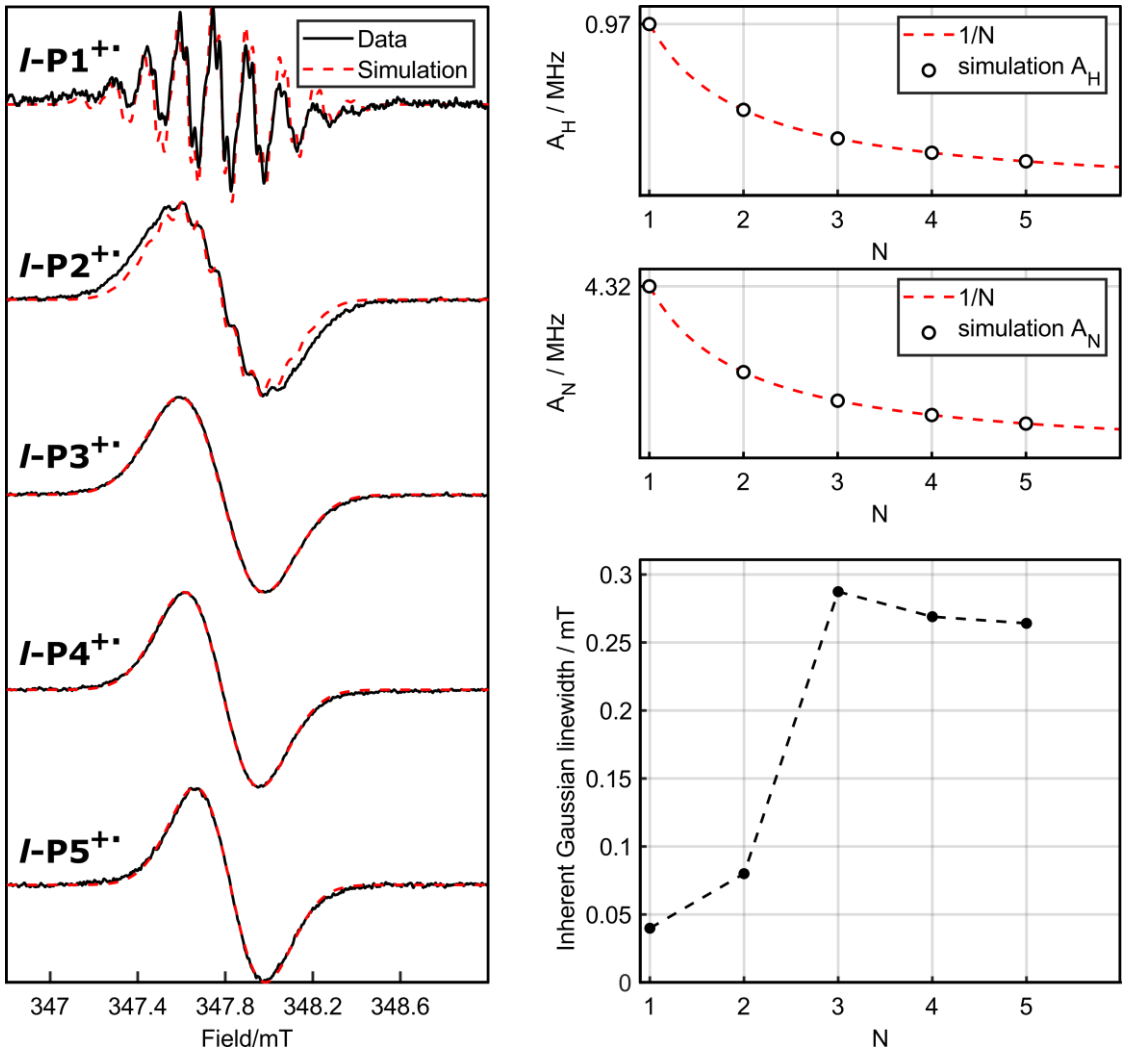

Figure S14. Numerical spectral simulations of the room temperature X-band cw-EPR spectra of the radical cations of the linear porphyrin oligomers up to the ***l*-P5**$^{+\bullet}$ using a Gaussian inherent linewidth. The procedure is the same as explained in the caption to Figure S13. As can be seen, a Gaussian function does not produce as good a fit to the spectrum of the monomer and dimer as a Lorentzian, but the same overall trend is observed in the two sets of simulations.

Another possibility for the breakdown of Equation 1 is that the spin density is not uniformly distributed over the oligomer chain length (at constant inherent linewidth). To test this possibility a further set of numerical simulations was performed in which the inherent linewidth was kept constant (and equal to the one determined for the monomer) whilst the hyperfine couplings to *N* sets of 4 equivalent ^{14}N nuclei were fitted for each oligomer. The simulated spectra together with the obtained delocalization pattern are shown in Figure S15. It is important to note that although these simulations are clearly consistent with non-uniformity in the spin density distribution, the obtained delocalization pattern cannot be uniquely assigned to the molecular structure. This is because the calculated spectrum is identical regardless of how the *N* sets of equivalent couplings are distributed over the oligomer molecule. The spin densities obtained from these simulations are, however, comparable with the spin densities obtained using DFT for the nitrogen nuclei as will be discussed in the following sections.

An equivalent set of simulations on the data for the butadiyne-linked oligomer series investigated previously converges on a uniform spin density distribution with an approximately constant inherent linewidth for all the oligomers.[8,9] As mentioned in the main

text, the structural similarity between the two oligomer series implies that the factors which influence the inherent linewidths of the EPR transitions should be present in an equal proportion in both series of oligomers. As such, we can conclude that the trend in inherent linewidth determined in Figure S13 is not a correct representation of the experimental spectra. Moreover, the non-uniform spin densities in Figure S15 allow us to simulate with reasonable accuracy the ethyne data using the same inherent linewidth for all the oligomers.

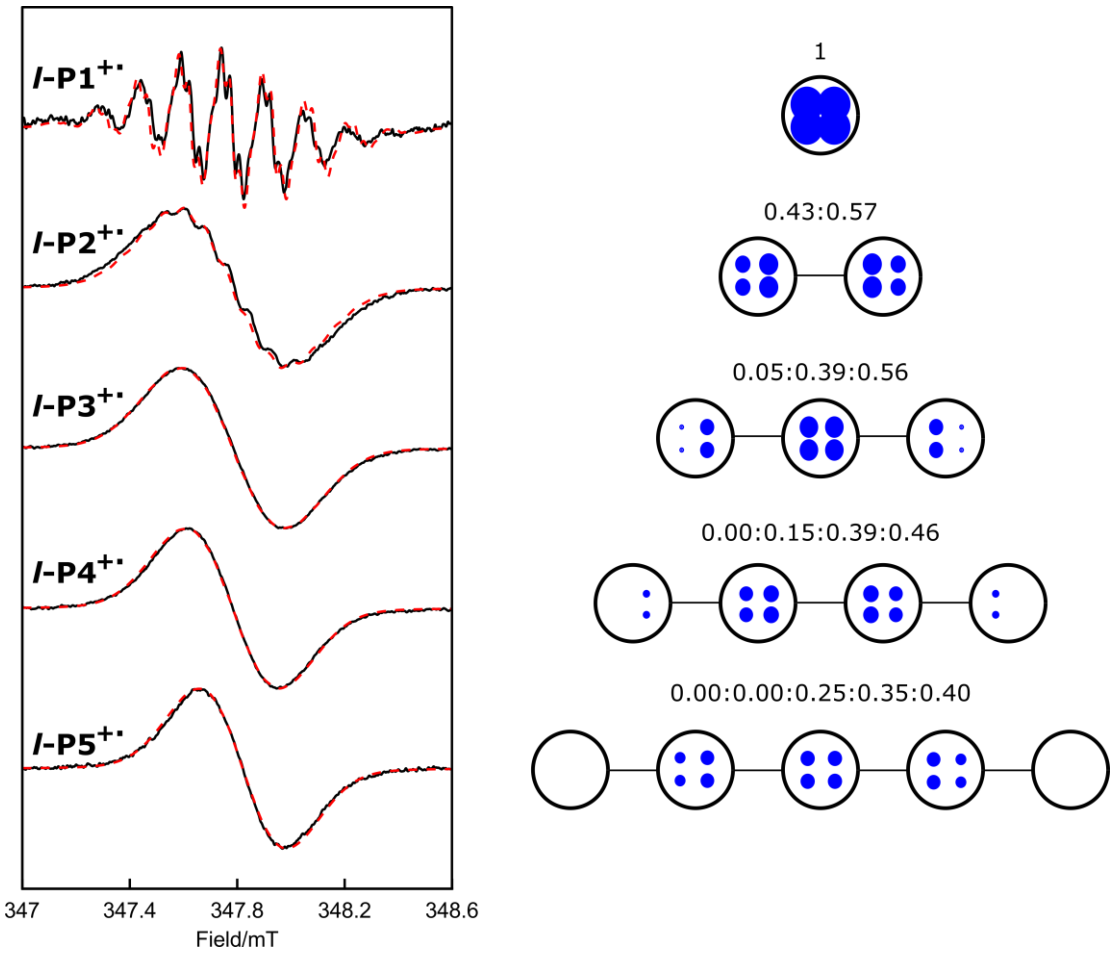

Figure S15. Numerical spectral simulations (red dashed lines) of the room temperature X-band cw-EPR spectra (black lines) of the radical cations of the linear porphyrin oligomers up to the ***l*-P5**$^{+\bullet}$ obtained by fitting a set of numbers (right) representing a non-uniform spin density on ***N*** sets of 4 equivalent nitrogen nuclei. The inherent linewidth of the lines was kept constant and equal to the value determined for the monomer (as shown in Figure S13). The fitting converges on a non-uniform spin density. However, these spin densities cannot be assigned uniquely to particular nitrogen nuclei of the real oligomer structure.

DFT computed spin densities

Method

The Gaussian16 package was used for optimizing the geometries of the radical cations of the linear oligomers ***l*-P*N*$^{+\bullet}$** and the ring ***c*-P6·T6$^{+\bullet}$** as well as for computing the Mulliken spin densities necessary for simulating the EPR spectra.[10] The basis set was chosen to be def2SVP for the H, C, and N centers, whereas def2-TZVP was used for the Zn centers. The functional was B3LYP in all calculations. The aryl side-groups as well as the protecting groups on the terminal ethynes were replaced with protons in order to increase the computational speed of the geometry optimization. The resulting structures are consistent with previous DFT geometry optimizations and, as shown in Figure S16, the linear oligomers have a dihedral angle of ~20° between adjacent porphyrin units. [2]

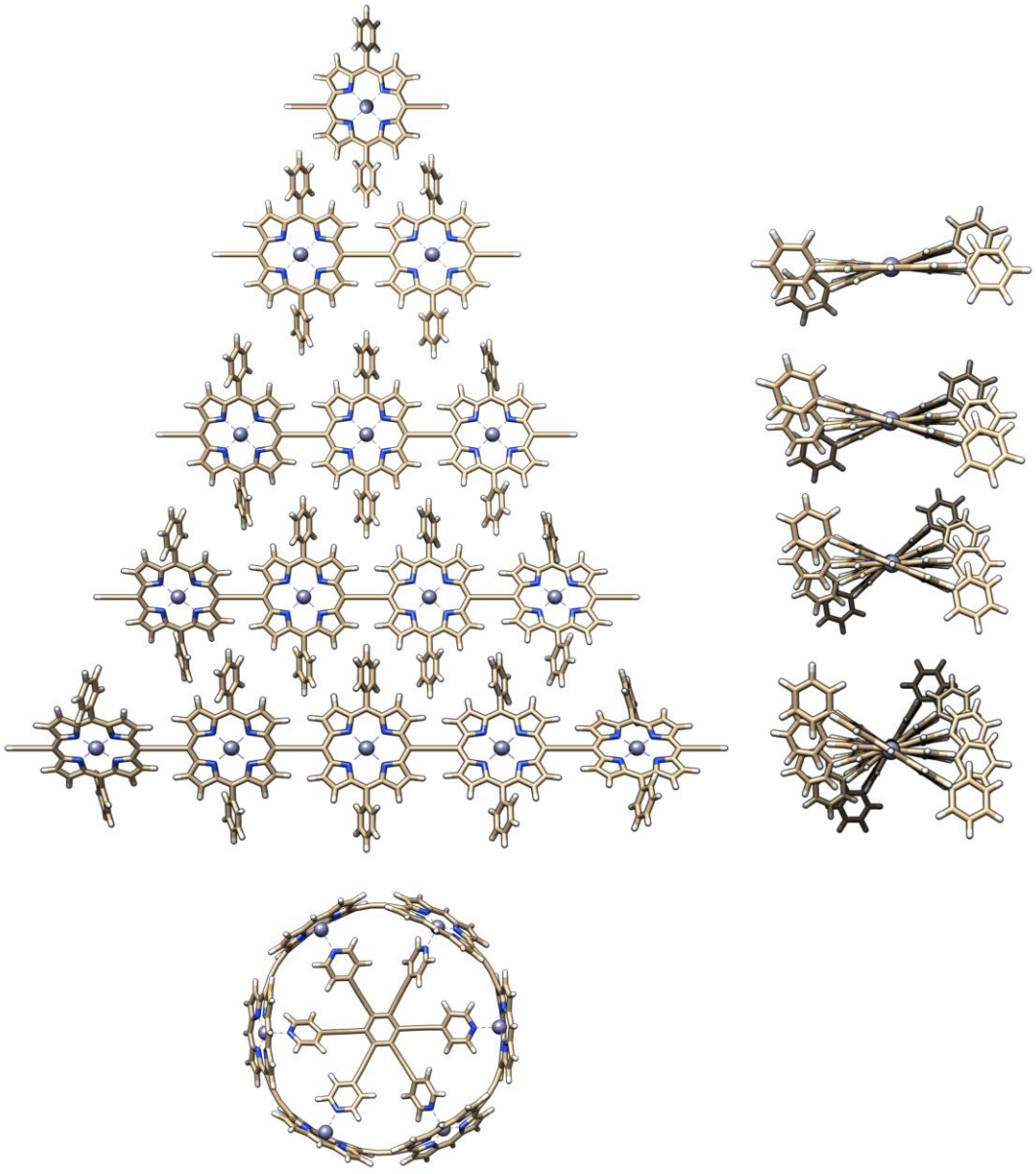

Figure S16. Top-view of the DFT optimized structures of the oligomers ***l*-P*N*$^{+\bullet}$** and the ring ***c*-P6·T6$^{+\bullet}$** (left). Side-view of the linear oligomers with $\boldsymbol{N = 2 - 5}$ (right).

^{14}N spin density for the ethyne-linked oligomers

The cw-EPR spectra presented in this work have a hyperfine structure which is attributed mainly to the ^{14}N nuclei of the porphyrin units. Since the cw-EPR spectra were acquired at room temperature, the observed couplings can be treated as isotropic with a magnitude proportional to the Mulliken spin density on the nitrogen atoms:

$$A_i = c\rho_i$$

The equation above is the McConnel relationship which states that the hyperfine coupling to a particular nucleus, A_i, is related to the spin density on that nucleus, ρ_i, via a proportionality constant, c, referred to as the McConnel constant. In order to obtain the DFT predicted EPR spectra presented in Figure 2 of the main text, the McConnel constant was determined from the EPR spectrum of the monomer.

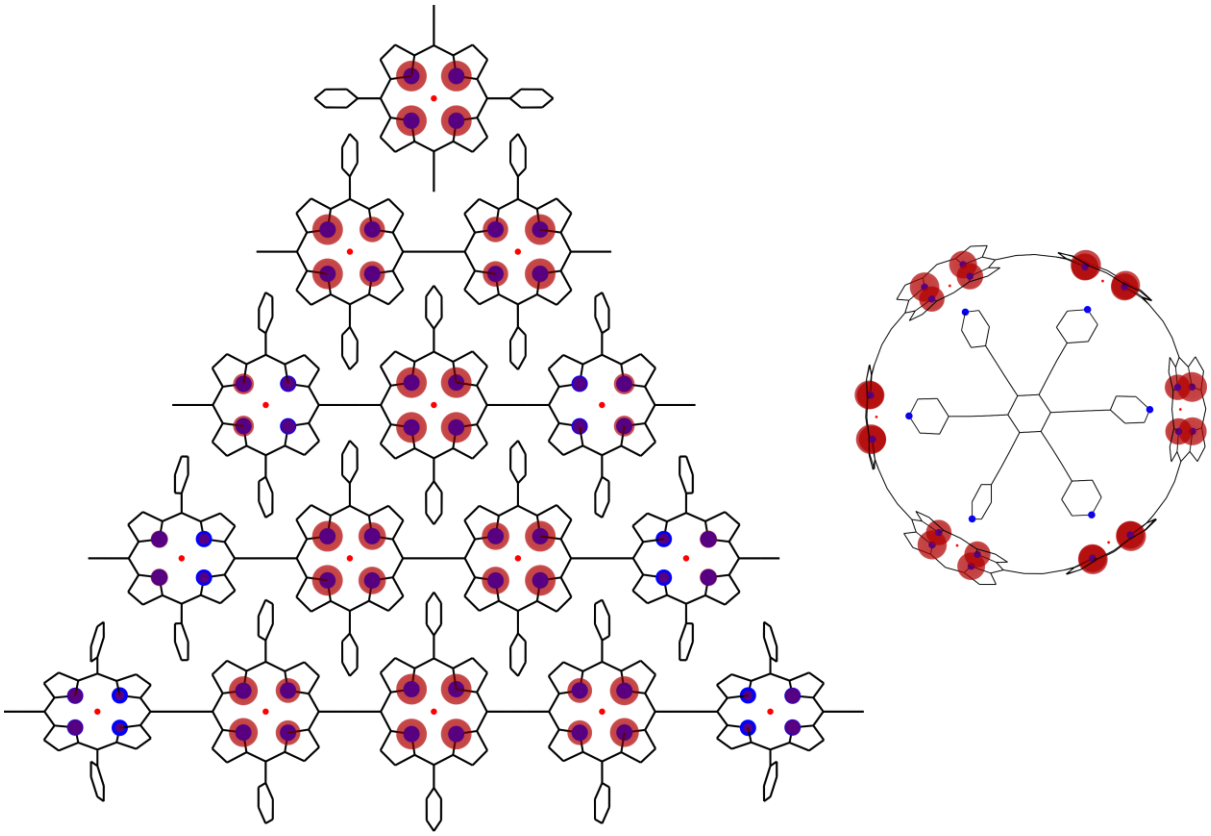

Figure S17. DFT computed Mulliken spin density on the ^{14}N nuclei of the radical cations of the ethyne-linked linear porphyrin oligomers ***l*-PN**$^{+\bullet}$ and the ring ***c*-P6·T6**$^{+\bullet}$. The spin density on a particular nucleus is represented as a red sphere centered on the nucleus with a radius proportional to the magnitude of the spin density. The magnitudes of the spin densities have been re-normalized (to the maximum) to allow visualization of the spin densities on the larger oligomers. Note on the color code: the blue circles represent the positions of the ^{14}N nuclei and the red circles the spin density.

More precisely, the monomer spectrum was fitted using EasySpin to obtain the hyperfine coupling to the four equivalent ^{14}N nuclei as well as the inherent linewidth. By contrast with the simulations presented in the previous section, in this case, the proton couplings were treated as being part of the inherent Lorentzian linewidth and they were not explicitly included in the simulations. The proton couplings were neglected in order to ease the computational cost of simulating using the large numbers of small DFT spin densities on all

the protons (at least 14 non-equivalent protons need to be included just for the monomer). However, neglecting the protons only has an influence on the super-hyperfine structure of the monomer spectrum, but it does not change the overall linewidth of the Gaussian envelope, and it is insignificant for the larger oligomers. The McConnel constant was then determined by dividing this hyperfine coupling by the ^{14}N spin density determined from the monomer DFT result illustrated in the top of Figure S17. As such, we determined $c = 51.25$ MHz and an inherent Lorentzian linewidth of 0.12 mT. These values were then used together with the ^{14}N Mulliken spin densities obtained from DFT to obtain the DFT predicted spectra in Figure 2 of the main text. These spectra were then analyzed in the same manner as the experimental spectra to yield the trend in the linewidth of the spectral envelope (shown in Figure 2 of the main text and Figure S19). The Mulliken spin densities on all the atoms together with the optimized geometries are provided as separate text files.

^{14}N spin density for the butadiyne-linked oligomers

The spin density for the linear oligomers of the butadiyne-linked oligomers was evaluated using the same DFT parameters as detailed above. The resulting Mulliken spin densities on the ^{14}N nuclei are shown in Figure S18 and the total spin density and structure files are provided as text files. By comparing with the results in Figure S17, it is apparent that, for both series, DFT predicts a non-uniformly distributed spin density on the ^{14}N nuclei.

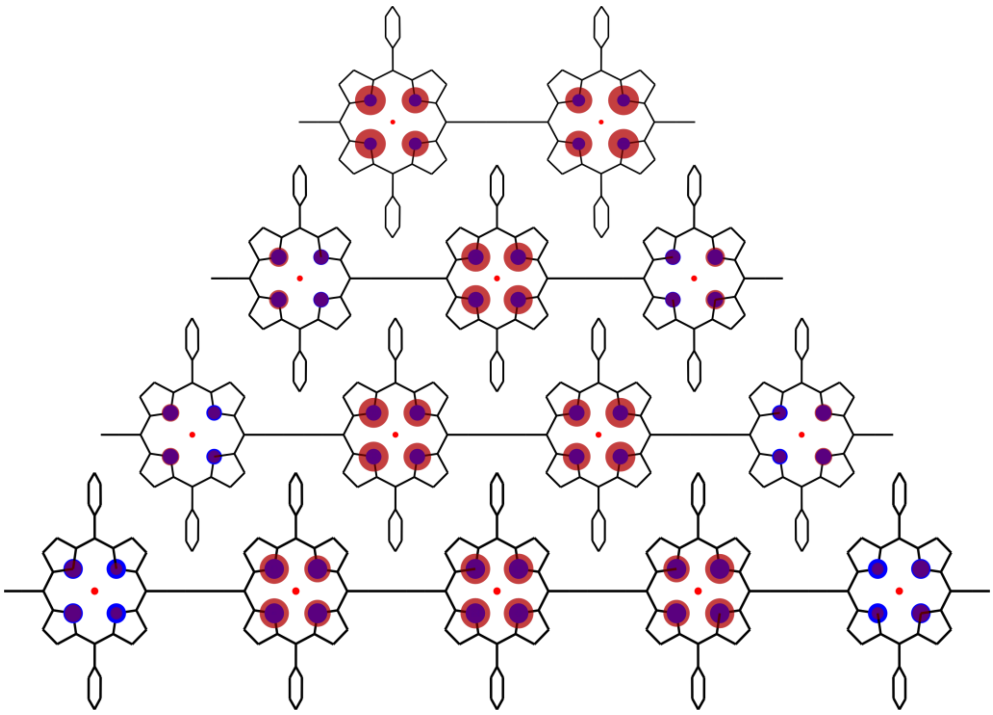

Figure S18. DFT computed Mulliken spin density on the ^{14}N nuclei of the radical cations of the butadiyne-linked linear porphyrin oligomers with $\boldsymbol{N = 2 - 5}$**.** Note on the color code: the blue circles represent the positions of the ^{14}N nuclei and the red circles the spin density.

However, using the same McConnel constant and inherent Lorentzian linewidth as we determined in the previous section, we can obtain a set of DFT-predicted cw-EPR spectra for the butadiyne-linked oligomers. The resulting spectra and envelope linewidths are compared between the two oligomer series in Figure S19. As can be seen, the DFT spin density (for the optimized geometry) seems to be a better representation of the experimental trend for the ethyne-linked oligomers. Nevertheless, the result for the butadiyne-linked series also shows good agreement with experiment. The DFT predicted envelope linewidth for the

butadiyne-linked series deviates significantly less from Equation 1, similarly to the butadiyne-linked experimental trend in linewidth.

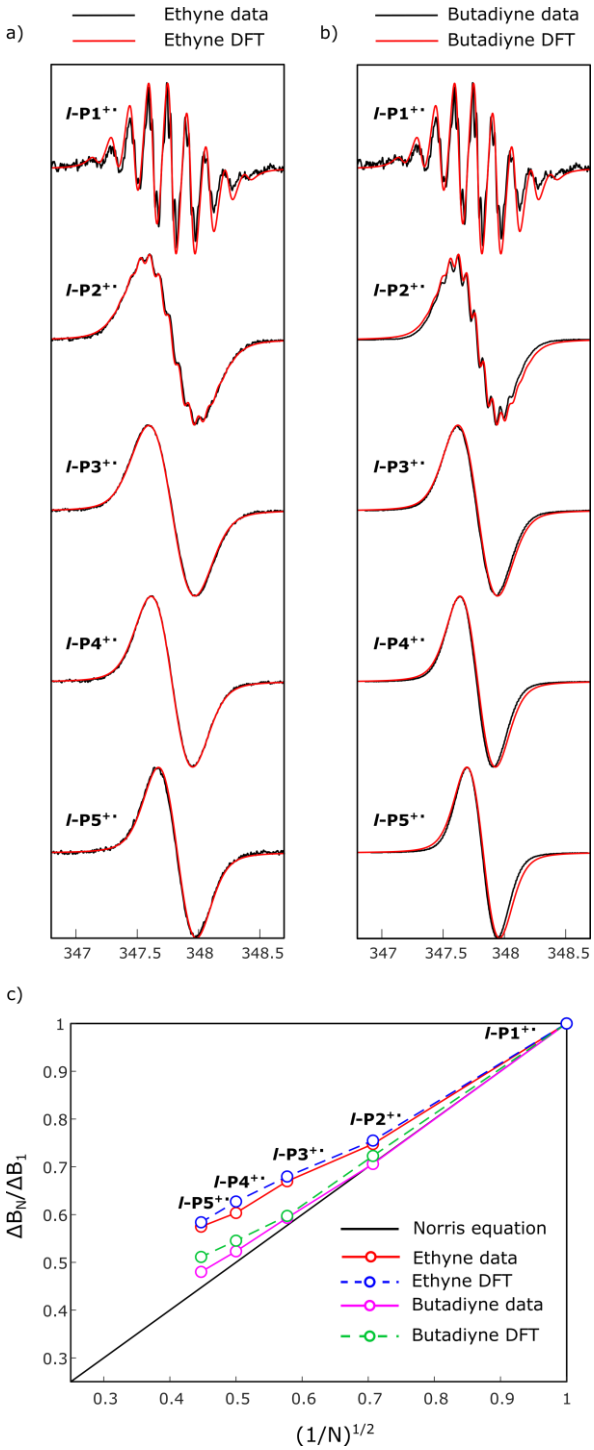

Figure S19. (a) Experimental and DFT predicted cw-EPR spectra for the ethyne-linked linear oligomers. (b) Experimental and DFT predicted cw-EPR spectra for the butadiyne-linked linear oligomers. (c) Comparison of the experimental and DFT-predicted trend in envelope linewidth between the ethyne- and butadiyne-linked series of linear porphyrin oligomers. The experimental spectra and envelope linewidths for the butadiyne oligomers were adapted from reference [8].

Given the spin densities and comparative trends illustrated in Figures S17, S18 and S19 we can conclude that the extent of delocalization of the spin density for the ethyne-linked series of oligomers is described fairly accurately by a static (time-independent) spin density for all the oligomers. For the butadiyne-linked series, the static spin density obtained from

DFT is not as good a representation of the experimental spectra but it predicts a trend in the envelope linewidth which is closer to the trend expected from Equation 1 (Figure S19(c)).

Dihedral angle dependence of ^{14}N spin density in dimers

By comparison with previous experimental and computational studies on similar porphyrin structures, it might be argued that the trends illustrated in Figure S19(c) could be caused by differences in inter-porphyrin dihedral angle distributions.[2,8,9] More precisely, it could be argued that for the butadiyne-linked series, the dihedral angle dependence of the ^{14}N spin densities is averaged to a unique characteristic value for all the ^{14}N nuclei in a porphyrin unit due to the fact that the barrier for rotation (minimum is at ~0° with a barrier in the neutral dimer of ~3 kJ mol^{-1}) is similar to the thermal-energy at room temperature (~2.5 kJ mol^{-1}). For the ethyne-linked series, the barrier for rotation is larger (~5.9 kJ mol^{-1} in the neutral dimer) and the minimum energy conformation corresponds to a dihedral angle of ~20°.[2] As a result one could expect this difference in energy profiles to be the reason for the slight disagreement between the DFT and experimental cw-EPR spectra of the butadiyne-linked series.

It should be noted here that for the cation dimers both rotational barriers are expected to be somewhat higher than for the corresponding neutral molecules so that full averaging of the couplings is unlikely. Here, we try to illustrate any effect of rotational averaging on the neutral dimers which should, qualitatively, parallel any such changes seen in their cations.

To do so, we calculated the spin density on the ^{14}N nuclei of the ethyne- and butadiyne-linked dimer as a function of the dihedral angle between the porphyrin units. The results of these calculations are summarized in Figure S20. We first note that in both dimers, for the equilibrium angle (~20° for ethyne and 0° for butadiyne), the spin density on the peripheral ^{14}N nuclei (ρ_P) is larger than the spin density on the central ^{14}N nuclei (ρ_C). For the butadiyne-linked dimer, we note that in the range 0 – 50° we have $\rho_C/\rho_P < 1$ whereas in the range 50 – 90° we have $\rho_C/\rho_P > 1$. This implies that, in an ensemble, we expect to find approximately just as many conformers with $\rho_P > \rho_C$ as conformers with $\rho_P < \rho_C$. This fact is further illustrated by the fact that the ratio of the thermally averaged spin densities, $\langle\rho_C\rangle/\langle\rho_p\rangle$, is ~0.98.

However, for the ethyne-linked dimer, Figure S20 reveals a different trend compared to the butadiyne case. We observe that the value of ρ_P is larger than ρ_C over a much wider range of dihedral angles (0 – 85°). Moreover, the ratio of the thermally averaged spin densities is $\langle\rho_C\rangle/\langle\rho_p\rangle = 0.91$. We believe that the difference in the ratio $\langle\rho_C\rangle/\langle\rho_p\rangle$ (which is, in essence, a measure of the non-uniformity of the spin density) between the two dimers is sufficient to cause a change in the appearance of the two cw-EPR spectra. This fact is illustrated by the two panels in the lower part of Figure S20. For a constant linewidth (equal to the experimentally determined one), we see that the red spectrum of the ethyne-linked dimer with a ratio of 0.98 between ρ_C and ρ_P is distinguishable (by inspection) from the black spectrum corresponding to $\rho_C/\rho_P = 1$ (uniform). For the butadiyne-linked dimer, the 0.98 distortion is not sufficient to clearly differentiate the spectrum from the uniform density simulation (within the limits of the chosen inherent linewidth).

Although the difference in the thermally averaged ratio of central and peripheral ^{14}N spin densities is sufficient to cause the cw-EPR spectrum of the ethyne-linked dimer to be different by inspection, the experimental deviation of the envelope linewidth shown in Figure

2 of the main text is much larger than the deviation illustrated in Figure S20. In reality, the width of the Gaussian envelope of the red trace in the lower left panel of Figure S20 is not sufficiently different from the width predicted by Equation 1 to account for the observed deviations of the experimental trend.

As a result of the above discussion, we can conclude that it is unlikely for the dihedral angle dependence of the ^{14}N spin density to be the sole cause of the observed deviations from Equation 1. It might be argued that for the longer ethyne-linked oligomers, the spin density of the ^{14}N nuclei does not average to a single characteristic value for all the ^{14}N nuclei, in line with the fact that the central and peripheral spin densities have a significantly more asymmetric dependence on dihedral angle (cf. left and right top panels of Figure S20). However, based on these calculations, the thermally averaged distortion in spin density is likely not to be sufficient to account for the experimental trend for the longer oligomers. We believe the deviations from Equation 1 observed for this series to be the result of the complex interplay between the static spin density (and its dependence on the dihedral angle) as well as the fact that on average there is a larger non-equivalence between central and peripheral ^{14}N spin density when the porphyrins are linked by ethyne groups.

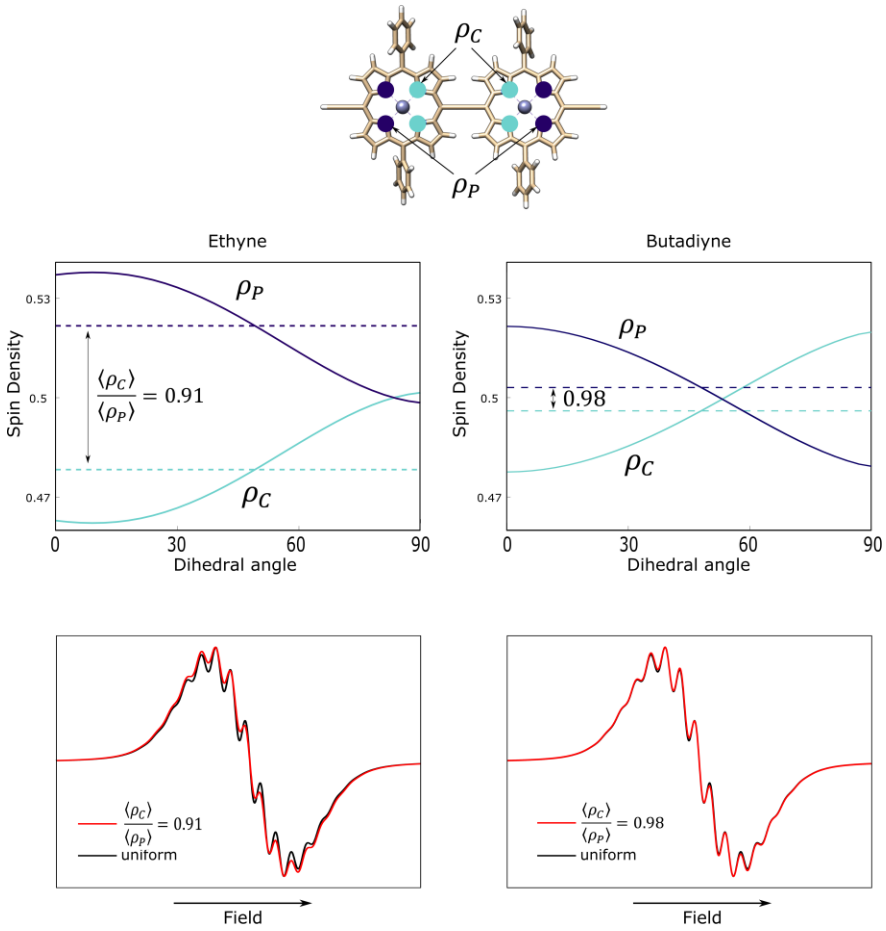

Figure S20. (Top) Dihedral angle dependence of the DFT predicted ^{14}N Mulliken spin density of the central and peripheral sets of equivalent nitrogen nuclei in the ethyne- (left) and butadiyne- (right) linked dimers. The dashed lines show the thermally averaged spin density. (Bottom) Simulations of the cw-EPR spectra with the corresponding thermally averaged ratio of spin densities (red) as well as the uniform case corresponding to $\boldsymbol{\rho_C/\rho_P = 1}$. The inherent linewidth was kept the same and equal to the value of 0.12 mT determined according to the discussion in the previous section.

^{1}H-ENDOR measurements and hyperfine coupling tensors

Experimental method

Pulse EPR experiments were carried out at 85 K at Q-band microwave frequencies (~34 GHz) on a Bruker Elexsys 580 spectrometer equipped with an Oxford Instruments gas flow cryostat. The Mims ENDOR spectra reported in the main text were acquired with the pulse sequence $\frac{\pi}{2} - \tau - \frac{\pi}{2} - T - \frac{\pi}{2} - echo$ with microwave pulse lengths of 44 ns and τ = 260 ns. A 16 μs radiofrequency π – pulse was applied during the mixing period, T. The power of the radiofrequency pulse was adjusted to form a π – pulse using a nutation experiment at the Larmor Frequency of ^{1}H (*ca.* 51 MHz) for the field position corresponding to the maximum echo intensity. The ENDOR spectra were recorded using different τ values in order to rule out the presence of distortions due to the blind-spots characteristic of the Mims ENDOR pulse sequence. Figure S21 presents a summary of all the recorded ^{1}H-ENDOR spectra.

Summary of experimental results

The ^{1}H-ENDOR spectra in Figure S21 are comprised of peaks centered at the Larmor frequency of ^{1}H and split by the hyperfine coupling constants of all the individual protons present in the molecule (weak coupling limit). As such, these spectra constitute a complementary set of experimental measurements of the spin density, and in particular, of the spin density on the ^{1}H nuclei. By contrast to the room temperature cw-EPR measurements, these ^{1}H-ENDOR spectra are acquired at cryogenic temperatures (85 K; necessary because of the fast T_2 relaxation times in liquid solutions) and as a result, the anisotropy of the hyperfine coupling interactions is resolved and the interpretation of the spectra is more complicated. A direct deconvolution of the monomer spectrum involves performing a simultaneous fit of 84 parameters corresponding to 3 eigenvalues and 3 Euler angles describing the hyperfine coupling tensor of each one of the 14 protons. As a consequence, a direct deconvolution of the spectra for the longer oligomers would involve a simultaneous fit of 84*N* independent parameters. Such an analysis is impractical, if not impossible, and as a result, a quantitative interpretation of these spectra relies on an *a priori* knowledge of the hyperfine coupling tensors (*e.g.* from DFT calculations; see next sections).

Nonetheless, there are a few conclusions to be drawn from a qualitative analysis of the shape of the ^{1}H-ENDOR spectra. Firstly, by comparing the spectra of the ethyne-linked monomer and dimer shown in Figure S21 (a), we see that the width of the dimer spectrum is no longer half the width of the monomer spectrum. This is in contrast with previously reported observations for the butadiyne-linked series.[8] The butadiyne-linked dimer spectrum (red line in Figure S21(c)) has half the width of the monomer spectrum, thus indicating complete delocalization of the proton spin density. The comparison in Figure S21 (c) between the butadiyne and ethyne-linked dimer ^{1}H-ENDOR spectra, reveals that in the ethyne-linked dimer there are two distinct groups of protons with hyperfine couplings of ~0.7 MHz and ~1.4MHz. This observation is in agreement with the previous discussion of the cw-EPR spectra whereby the ethyne linker causes distortions in the spin density leading to a non-uniform distribution which in turn causes groups of protons (or nitrogens for the cw-EPR spectra) to have larger hyperfine couplings (see next section).

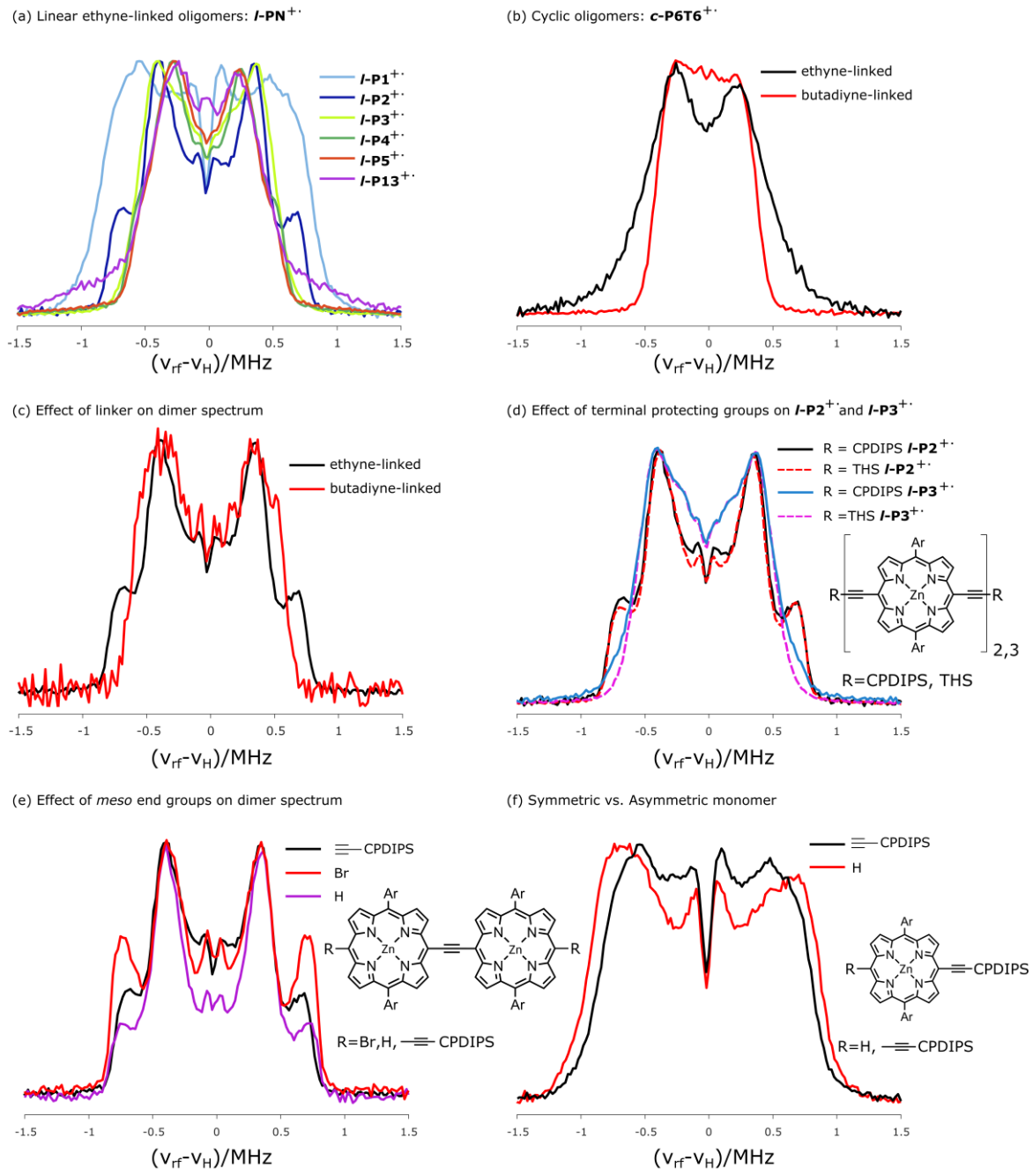

Figure S21. (a) ^{1}H-ENDOR spectra of the linear ethyne-linked oligomers ***l*-PN$^{+\bullet}$** with $N = 1-5, 13$. (b) Comparison of ^{1}H-ENDOR spectra of the ethyne- and butadiyne-linked cyclic hexamer structures. (c) Comparison of the ethyne- and butadiyne-linked dimer spectra. Note: the spectrum of the butadiyne-linked dimer is equivalent to the one reported by Peeks, Tait *et al*. using W-band (~95 GHz) microwave frequencies.[8] (d) Comparison of the effect of the terminal protecting groups on the ethyne groups of the dimer and trimer oligomers. Note: THS = trihexylsilyl, CPDIPS = cyanopropyl-diisopropyl-silyl. (e) Comparison of the effects of different end groups on the ^{1}H-ENDOR spectrum of the dimer. (f) The effect on the ^{1}H-ENDOR spectrum of replacing one of the *meso*-ethyne groups of ***l*-P1$^{+\bullet}$** by a proton.

Secondly, we notice in Figure S21 (b) that the spectrum of the ethyne-linked cyclic hexamer is broader than the corresponding spectrum of the corresponding butadiyne-linked ring. This, again, is consistent with the previous observations regarding the envelope linewidth of the room temperature cw-EPR spectra. The butadiyne-linked ring was shown previously to deviate slightly from Equation 1, but the linewidth of the ethyne-linked ring reported by us has a more pronounced deviation due to having a more distorted spin density distribution.[8]

Counter-intuitively, the distortions in spin density seem to be primarily related to the ethyne-linker and as such, the proximity of the porphyrin units, rather than the identity of the end-groups. For example, from Figure S21 (d) we see that the identity of the protecting groups of the terminal ethyne groups causes no change in the appearance of the ^{1}H-ENDOR spectra of the dimers and trimers. Moreover, replacing the terminal ethyne groups by hydrogen or bromine atoms, as shown in Figure S21 (e), merely changes the inherent width of the peaks in the dimer spectra but the magnitudes of the two types of hyperfine coupling remain the same. Interestingly, from Figure S21 (f) we see that removing one of the ethyne groups from the monomer and replacing it with a hydrogen atom has the effect of shifting the maxima in the ^{1}H-ENDOR spectra to larger values, indicating that the spin density is distributed non-uniformly (*i.e.* there are now groups of protons which have an enhanced hyperfine coupling) by comparison with the symmetric monomer. An equivalent effect was previously observed in the ^{1}H-ENDOR spectra of the photo-excited triplet state of symmetric and asymmetric porphyrin monomers and dimers.[11]

^{1}H spin densities and hyperfine coupling tensors

The above discussion of the ENDOR data is partially supported by a more theoretical approach to disentangling the contributions of individual groups of protons to the total spectrum. In an equivalent manner to how the ^{14}N Mulliken spin densities were used to evaluate the cw-EPR spectra, the ^{1}H spin densities can be used to evaluate the hyperfine coupling tensors. These tensor calculations were performed in ORCA on the previously shown geometries (Figure S16) using the B3LYP functional together with the EPR-II basis set.[12,13] The isotropic hyperfine coupling constants (*i.e.* the average of the eigenvalues of the hyperfine tensors) for the linear oligomers are shown pictorially in Figure S22 together with stick spectra superimposed on to the experimental ^{1}H-ENDOR spectra. As can be seen, the isotropic hyperfine coupling constants seem to over-estimate the observed narrowing of the ^{1}H-ENDOR spectra, especially for the oligomers with $N \geq 3$. Nevertheless, the monomer and dimer stick spectra qualitatively reproduce the experimental spectra. More precisely, it can be seen that for the monomer, there is a set of larger hyperfine couplings corresponding to the ortho- and para-phenyl protons of the aryl side chains, as well as a set of smaller couplings to the porphyrin protons. By contrast, the majority of the largest hyperfine couplings in the dimer belong to porphyrin protons, and especially to the protons close to the inter-porphyrin linker (which, according to this analysis, can be assigned to the shoulders in the experimental ^{1}H-ENDOR spectrum of the dimer). Given these results, it would seem that the monomer and dimer ^{1}H-ENDOR spectra should not be interpreted in terms of the observed narrowing of the width of the spectrum because the couplings do not correspond to comparable groups of protons.

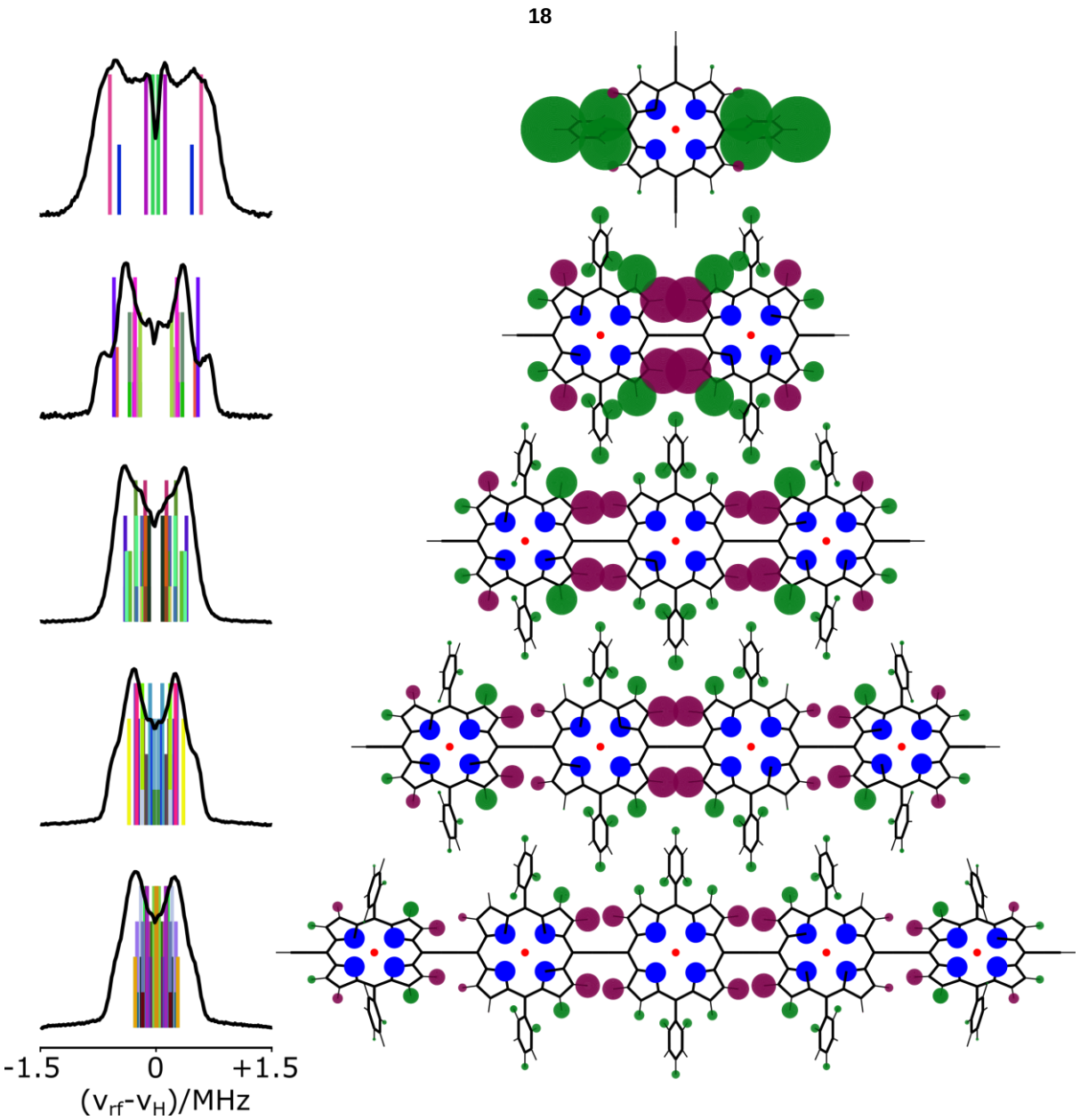

Figure S22. (Left) Stick spectra corresponding to the isotropic ^{1}H hyperfine couplings. The experimental ^{1}H-ENDOR spectra are superimposed on top of the stick spectra. (Right) The DFT computed isotropic ^{1}H hyperfine couplings of the linear oligomers represented as spheres with a radius proportional to the magnitude of the coupling. The green and purple colors refer to positive and negative values, respectively. The blue circles refer to the positions of the ^{14}N nuclei.

As mentioned before, the anisotropy of the hyperfine couplings is very likely to play an important role in the appearance of these low-temperature ^{1}H-ENDOR spectra. Figure S23 shows the DFT computed hyperfine coupling tensors as well as the ^{1}H-ENDOR spectra predicted from these tensors. The spectra were generated separately for each proton (red lines in Figure S21) with the *saffron* function in EasySpin using the experimental parameters outlined above, as well as an inherent linewidth of 0.25 MHz. The final spectrum is a sum of all the individual proton spectra and is shown in blue in Figure S23. These DFT predicted ^{1}H-ENDOR spectra seem to qualitatively reproduce the appearance of the experimental spectra. However, the width of the predicted spectra (evaluated as the peak-to-peak distance of the best-fit bimodal Gaussian distribution) is not a perfect match to the

experimental spectra, as can be seen in Figure S24. The reason behind this mismatch could be the fact that these simulations are neglecting the effect of anisotropic broadening (*i.e*. a broadening due to a distribution of the hyperfine coupling tensor eigenvalues and orientations). Nonetheless, the simulations with all the tensors explicitly included gives better results compared to an analysis based simply on the average spin density or the isotropic hyperfine coupling values (Figure S22). Ultimately, we see in Figure S24 that neither the DFT spectra, average spin densities, nor experimental spectra show the $1/N$ trend predicted for a complete and uniform delocalization of the spin density.

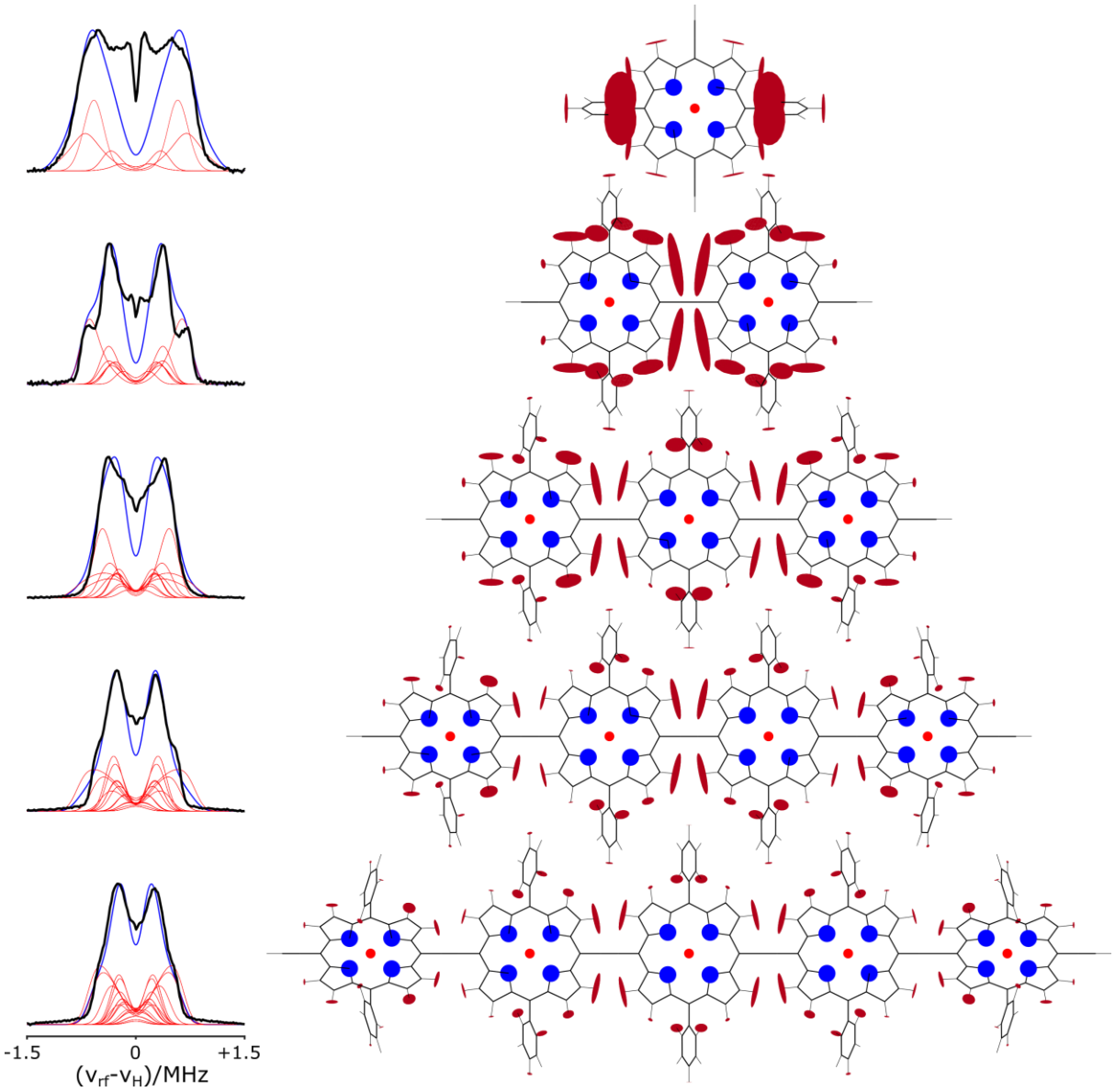

Figure S23. (Left) Simulated ^{1}H-ENDOR spectra of all the individual proton hyperfine coupling tensors taken separately (red lines). The blue line is the sum of the spectra of the individual protons and it is shown together with the experimental spectrum (black). (Right) Pictorial representation of the hyperfine coupling tensors as ellipsoids centered at the position of the corresponding proton with characteristic radii proportional to the eigenvalues of the hyperfine tensors and an orientation given by the corresponding Euler angles.

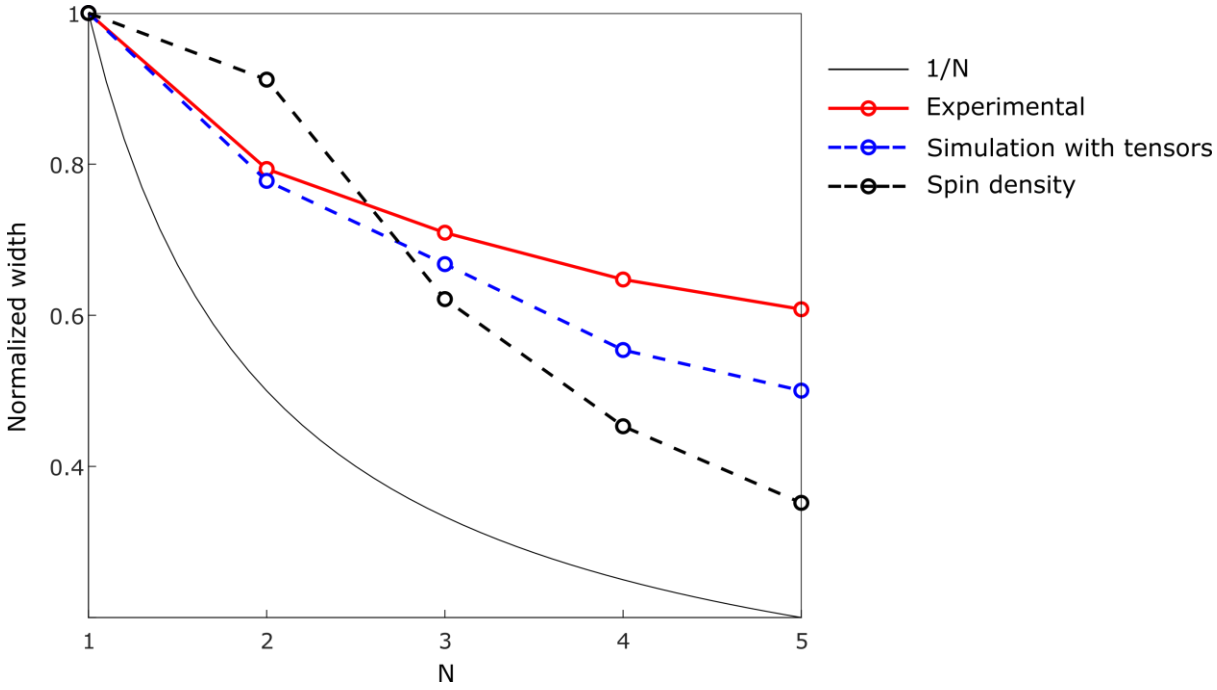

Figure S24. Comparison of the widths of the experimental and DFT-predicted ^{1}H-ENDOR spectra evaluated as the peak-to-peak distance obtained by fitting a bimodal Gaussian distribution to the spectrum. The trend in the average proton isotropic hyperfine couplings is also displayed for comparison with the $1/N$ expected trend for a completely and uniformly delocalized spin density.

References

[1] Haver, R.; Tejerina, L.; Jiang, H.-W.; Rickhaus, M.; Jirasek, M.; Grübner, I.; Eggimann, H. J.; Herz, L. M.; Anderson, H. L. Tuning the Circumference of Six-Porphyrin Nanorings. *J. Am. Chem. Soc.* **2019**, *141*, 7965.

[2] Rickhaus, M.; Vargas Jentzsch, A.; Tejerina, L.; Gruebner, I.; Jirasek, M.; Claridge, T. D. W.; Anderson, H. L. Single-Acetylene Linked Porphyrin Nanorings. *J. Am. Chem. Soc.* **2017**, *139*, 16502–16505.

[3] Parkinson, P.; Knappke, C. E. I.; Kamonsutthipaijit, N.; Sirithip, K.; Matichak, J. D.; Anderson, H. L.; Herz, L. M. Ultrafast energy transfer in biomimetic multistrand nanorings. *J. Am. Chem. Soc.* **2014**, *136*, 8217–8220.

[4] Norris, J. R.; Uphaus, R. A.; Crespi, H. L.; Katz, J. J. Electron spin resonance of chlorophyll and the origin of signal I in photosynthesis. *Proc. Natl. Acad. Sci. U.S.A.* **1971**, *68*, 625.

[5] Susumu, K.; Frail, P. R.; Angiolillo P. J.; Therien, M. J. Conjugated chromophore arrays with unusually large hole polaron delocalization lengths. *J. Am. Chem. Soc.* **2006**, *128*, 8380.

[6] MATLAB Release R2018B, The MathWorks, Inc., Natick, Massachusetts, United States.

[7] Stoll, S.; Schweiger, A. EasySpin, a comprehensive software package for spectral simulation and analysis in EPR. *J. Mag. Res.* **2006**, 178, 42.

[8] Peeks, M. D.; Tait, C. E.; Neuhaus, P.; Fischer, G. M.; Hoffmann, M.; Haver, R.; Cnossen, A.; Harmer, J. R.; Timmel, C. R.; Anderson, H. L. Electronic delocalization in the radical cations of porphyrin oligomer molecular wires. *J. Am. Chem. Soc.* **2017**, *139*, 10461.

[9] Tait, C. E. Ph.D. Thesis, Electron paramagnetic resonance studies of artificial supramolecular porphyrin structures and biological systems, University of Oxford, 2015.

[10] Frisch, M. J.; Trucks, G. W.; Schlegel H. B.; Scuseria, G. E.; Robb M. A.; Cheeseman J. R.; Scalmani, G.; Barone, V.; Petersson, G. A.; Nakatsuji, H.; Li, X.; Caricato, M.; Marenich, A. V.; Bloino, J.; Janesko, B. G.; Gomperts, R.; Mennucci B.; Hratchian, H. P.; Ortiz, J. V.; Izmaylov, A. F.; Sonnenberg, J. L.; Williams-Young, D.; Ding, F.; Lipparini, F.; Egidi, F.; Rega, N.; Zheng, G.; Liang, W.; Hada, M.; Ehara, M.; Toyota, K.; Fukuda, R.; Hasegawa, J.; Ishida, M.; Nakajima, T.; Honda, Y.; Kitao, O.; Nakai, H.; Vreven, T.; Throssell, K.; Montgomery Jr., J. A.; Peralta, J. E.; Ogliaro, F.; Bearpark, M. J.; Heyd, J. J.; Brothers, E. N.; Kudin, K. N.; Staroverov, V. N.; Keith, T. A.; Kobayashi, R.; Normand, J.; Raghavachari, K.; Rendell, A. P.; Burant, J. C.; Iyengar, S. S.; Tomasi, J.; Cossi, M.; Millam, J. M.; Klene, M.; Adamo, C.; Cammi, R.; Ochterski, J. W.; Martin, R. L.; Morokuma, K.; Farkas, O.; Foresman, J. B.; Fox, D. J. Gaussian 16, Revision A.03, Gaussian Inc.: Wallingford CT 2016.

[11] Richert, S.; Bullard, G.; Rawson, J.; Angiolillo, P. J.; Therien, M. J.; Timmel C. R. On the importance of electronic symmetry for triplet state delocalization. *J. Am. Chem. Soc.* **2017**, *139*, 5301.

[12] Neese, F. The ORCA program system, Wiley Interdiscip. Rev.: Comput. Mol. Sci. 2012, 2, 73.

[13] Barone V. in Recent Advances in Density Functional Methods, Part 1 (ed. D. P. Chong), World Scientific, Singapore, 1995, 287.